Controller Design and Analysis for Grid-Forming Inverter

Grid-Forming インバータの制御系設計および解析

by

Ko OUE

A Thesis Submitted to Doshisha University, Kyoto, Japan

for the Degree of Doctor of Engineering

November 15, 2022

Abstract

In the near future, power converters will be introduced into transmission grids on a large scale due to the increase of renewable energy sources. The control schemes of grid-connected inverters currently assume that there are sufficient synchronous generators (SGs) in the grid for the synchronization and integration of electric power. These inverters are called "grid-following" inverters. However, when grid-connected inverters significantly outnumber SGs, there is a need for the "grid-forming" inverters to operate the transmission grid autonomously. These inverters should generate AC voltages, share power with each other, and emulate the inertia effect like SGs do.

To satisfy these requirements, different control schemes for grid-forming inverters have been proposed in the literature, such as the droop control, virtual synchronous generator, and synchronverter for power control, and the cascaded PI controller for voltage regulation. This dissertation proposes two control schemes for grid-forming inverters.

The first control scheme is based on the dq domain for power and voltage control. The cascaded PI controller has often been used for voltage regulation. However, it is difficult to tune the control gains because of system couplings and the controller's bandwidths. This dissertation proposes a new controller based on a linear quadratic regulator (LQR) for voltage regulation and presents comparisons of the performances between them by simulations. It is also well known that instability due to interactions between the grid-connected inverter and the grid is sometimes observed. The stability is thus compared for the grid-forming inverters with both the cascaded PI controller and the LQR by eigenvalue analysis and the impedance method.

The second control scheme is based on the $\alpha\beta$-domain. With this controller, active and reactive powers can be controlled according to simple complex power control principles described only in the $\alpha\beta$-domain. The control system is described based on complex vector theory, which models the system as a single input single output (SISO) model so that the controller design is easier than dq- or $\alpha\beta$-multiple inputs multiple outputs (MIMO) models. Controller gain tuning for both the outer power and the inner voltage regulator is also proposed. The power control gains are tuned based on transfer functions around an operating point and the voltage regulator is tuned by the LQR. The proposed control method is investigated and validated by simulations with a C control program and by experiments with a DSP-based digital control system.

Contents

List of Figures

List of Tables

List of Acronyms

AC	Alternative Current
CVRC	Complex Vector Resonance Controller
DC	Direct Current
DSP	Digital Signal Processor
FOC	Fractional Order Controller
GHG	Greenhous Gas
LPV	Linear Parameter Varying
LTI	Linear Time-Invariant
LQR	Linear Quadratic Regulator
MG	Micro-Grid
MIMO	Multiple Inputs and Multiple Outputs
PCC	Point of Common Coupling
PI	Proportional and Integral
PLL	Phase-Locked Loop
PWM	Pulse Width Modulation
RES	Renewable Energy Source
SG	Synchronous Generator
SISO	Single Input and Single Output
SS	Storage System
VSM	Virtual Synchronous Machine

1. Introduction

1.1 Context and motivation

For environmental reasons, more than 150 countries including Japan have declared that they will realize carbon-neutrality by 2050 [1]. To achieve zero greenhouse gas (GHG) emissions, it is essential to introduce a large amount of storage systems (SSs) and renewable energy sources (RESs), such as solar photovoltaics (PVs) and wind farms, and to reduce the reliance on energy from fossil fuels. From another point of view, energy security is also strengthened with the expansion of the electricity supply from RESs, and this is independent of the global situations.

Over the last decade, the capacity of RESs in Japan has expanded from 20 to over 80 million kilowatts and this rapid expansion is expected to continue for the next decade [1][2]. With the increased application of RESs and SSs, massive power electronic converters will be interfaced with alternative grids [3]. These converters are now controlled under the presumption that SGs dominate in the grid and establish a nominal voltage amplitude and frequency that allow converters to synchronize with AC voltage at the point common coupling (PCC) by phase-locked loop (PLL) or zero-crossing detection techniques. These converters are called “grid-following” converters [4].

However, as the share of grid-following inverters is growing rapidly, some grids will be possibly operated with few or no SGs. In these cases, conventional grid-following inverters are not able to inject power into the grid due to the functions of synchronization. Moreover, due to the massive introduction of grid-following inverters, the ratio of the power supply from SGs is decreased, which results in the reduction of total inertia in the grid. Consequently, it becomes more difficult to stabilize the frequency in the event of fault or large load fluctuations due to faster dynamic responses of frequency [1], and this has already been noticed in several European areas [5]. For autonomous operation, the control principle of grid-connected inverters will no longer need to follow the grid but instead will lead the grid. Grid-connected inverters based on this concept are called “grid-forming” inverters [3][4].

It is widely known that interactions among grid-connected inverters and grid impedances may destabilize the inverter control loops and lead to oscillations [6]. This issue becomes severe with higher penetration of grid-connected inverters [7]. Some incidents of destabilization due to undesired harmonics and resonances have been reported in [8]-[10]. Hence, it is essential to find ways to analyze the stability of inverter-based grids and embed them into the design process of inverter controls.

To meet these challenges, this dissertation mainly focuses on controller designs of “grid-forming” inverters and stability analysis. Two controller structures and tuning methods are proposed and their stabilities are then analyzed in different ways.

1.2 State of the art

1.2.1 Grid-following control

The grid-following inverter control assumes that SGs dominate in the grid and establish a stiff nominal voltage amplitude and frequency. Its objective is to ensure the injection of a reference current, which is synchronized with the grid voltage at the PCC and is derived from reference active and reactive powers, into the grid. Fig. 1-1 shows a basic control structure of a three-phase grid-following inverter. The inverter is connected to the grid through an LCL filter that attenuates switching harmonics. It has a current controller to behave as a current source, and the synchronization function is implemented by PLL [11] or zero-crossing technique [12].

This controller is based on the *dq*-frame, the amplitude of $v_{q,pcc}$ has a null value thanks to the PLL or the zero-crossing, while $v_{d,pcc}$ is equal to the amplitude of the grid voltage. p_{ref} and q_{ref} are the reference active and reactive powers, respectively, and the current i_{od} controls the active power, while i_{oq} controls the reactive power. The current control is accomplished through the use of a proportional and integral (PI) controller and a decoupling control. To reduce harmonics of the injected current, the PI controllers are often replaced with proportional-resonant (PR) controllers. Another current tracking controller for the grid-following inverter has been proposed in the three-phase domain in [12]. Its difference from the PI control is that the Park transformation is not needed in the controller stage so the references are three-phase sinusoidal currents.

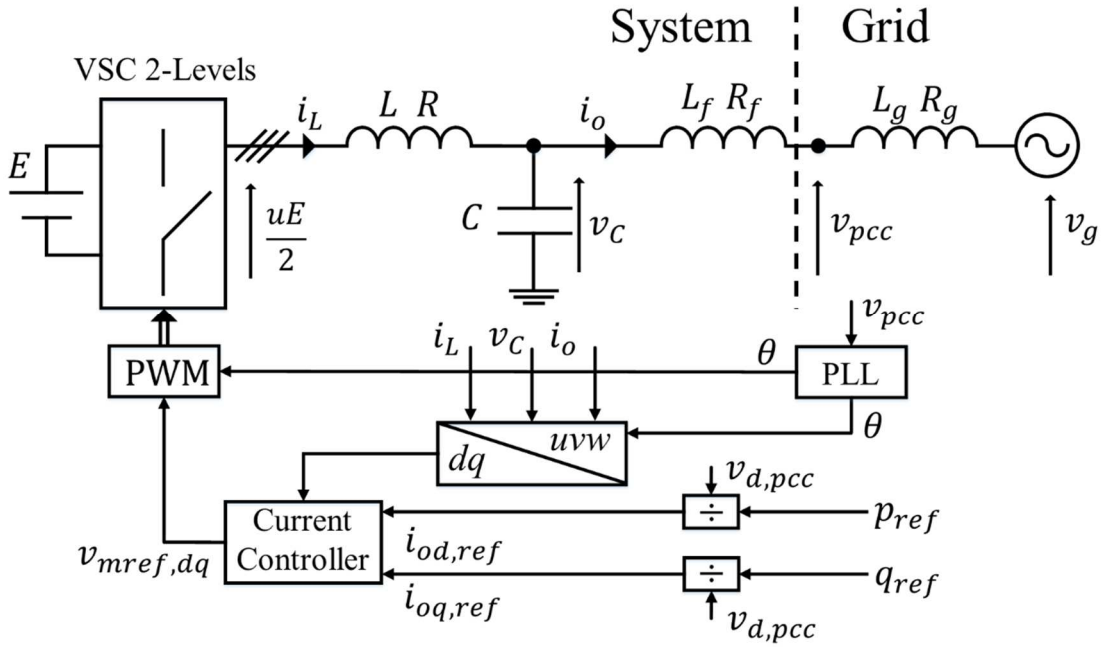

Fig. 1-1. Basic control structure for three-phase grid-following inverter.

Table 1-1. shows the concerns and their influences with high penetration of grid-following inverters. First, if they dominate the grid or a micro-grid (MG) area, and are disconnected from the main AC grid, they can no longer inject current (power) to the load due to the loss of followed AC voltage. Second, their high penetration, meaning the reduction of electric power provided from SGs that have mechanical inertia, causes decreases of total grid inertia. Consequently, this induces a faster dynamic response of the frequency and it is more difficult to stabilize the frequency under grid faults or large load fluctuations. Lastly, the grid voltage is sensitive to the current injection under the weak grid or high impedance grid and may exceed the threshold.

Table 1-1. Concerns and their influences with high penetration of grid-following inverters.

No.	Concerns	Influences
1	Loss of synchronism	Current (power) can no longer be injected to the grid due to the synchronization mechanism.
2	Decreases of total grid inertia	It causes a faster dynamic response of frequency, and frequency exceeds the threshold under grid faults or large load fluctuations.
3	Voltage fluctuations under weak grid	Grid voltage is sensitive to the controlled current under weak grid (high grid impedance) and exceeds the threshold.

1.2.2 Grid-forming control

Like SGs, the grid-connected inverters should be able to operate under any topology of the transmission grid, which is mainly divided into two topologies: grid-connected mode and islanded mode. In grid-connected mode, the inverters are connected through the PCC to an equivalent Thevenin source including other sources of electrical energy. In islanded mode, a passive load is only fed by sources interfaced by grid-connected inverters. There are two types of operations for islanded mode: standalone operation and parallel operation. In standalone operation, one inverter is responsible for supplying loads to establish a fixed voltage and frequency. In parallel operation, several inverters are operated in parallel, with or without communication. It is necessary to ensure that the power is shared according to the capacity of each source. An MG with 100% power electronics or uninterruptible power supply (UPS) lines-interactive converters are found in this operation. Grid-connected inverters must have a voltage source behavior to operate in the islanded mode. Grid-connected inverters that can operate in both grid-connected and islanded modes are called “grid-forming” inverters.

The penetration of grid-connected inverters is growing around the world. In some areas, such as Ireland and Germany, they have already reached very high levels and can occasionally be operated without SGs. The situation involving no SGs in the grid can occur. Even in this case, the grid must supply the same

quality as the electromechanical transmission grid. The grid-forming inverters must be able to supply the system with sinusoidal current of a given frequency, and must generate a fixed voltage at the PCC.

Table 1-2. Services required for an electrical system [13].

No.	Services	Conditions
1	Supply of AC currents	Frequency: $f_{min} < f < f_{max}$
2	Supply of all loads connected according to their nominal operation power	RMS voltage: $V_{min} < V < V_{max}$
3	Power sharing between parallel generators	Active power: $\Sigma P_{gen} = P_{load}$
4	Infrastructure security (overcurrent limitation)	Inverter current: $I < I_{max}$

Table 1-2 indicates the services that the electrical system including grid-forming inverters must guarantee like the system dominated SGs have done [13]. Unlike inverters, SGs have inertia and the frequency is determined by the rotation speed with slow dynamic. In contrast, the inverter's frequency is determined by its control principle, and its primary control can form virtual inertias and damping factors to the grid-forming inverters. The primary control also allows inverters to synchronize to the grid without detecting the grid-phase and to share power with other generators. Four well-known primary controls have been proposed in the literature: the synchronverter [14], the virtual synchronous machine (VSM) [15]-[19], the virtual oscillator [20], and the droop control [21]-[25].

Grid forming inverters are designed for autonomous operation to impose AC voltage and fix frequency, by balancing the generating power and loads. Fig. 1-2 shows the basic circuit diagram for a grid-forming inverter. The scheme of control consists of a primary control and multi-cascaded loop in the *dq* frame. The primary control is the droop control to share power with other generators and the control frequency. In the cascaded loop, the outer loop is responsible for voltage control, and the inner loop is responsible for current control.

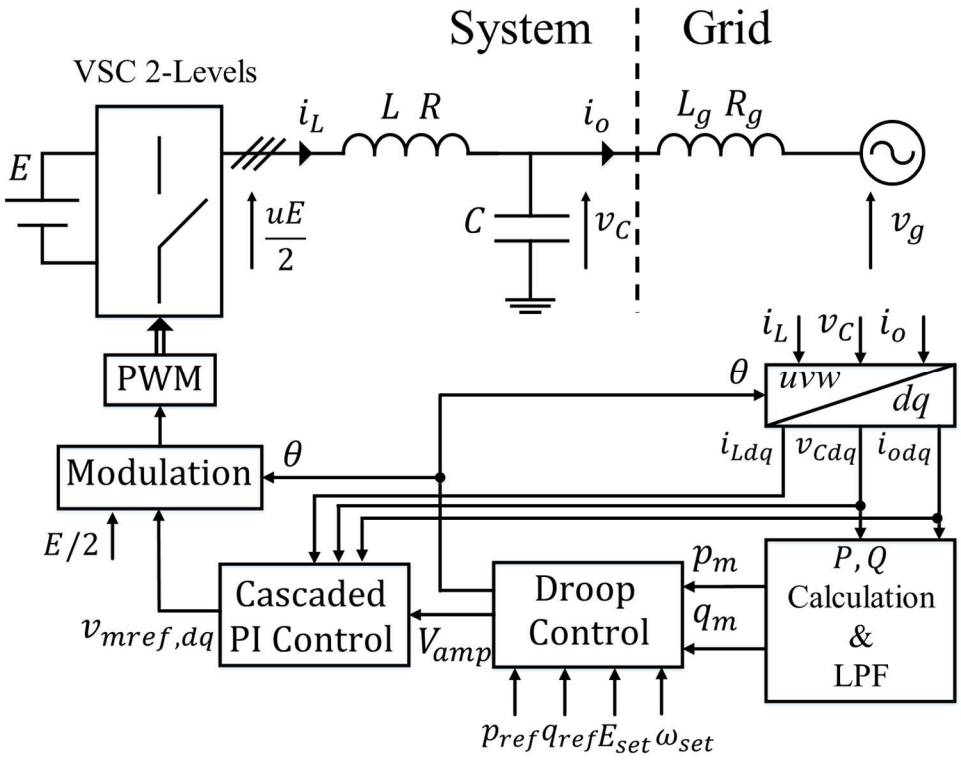

Fig. 1-2. Basic control structure for three-phase grid-forming inverter.

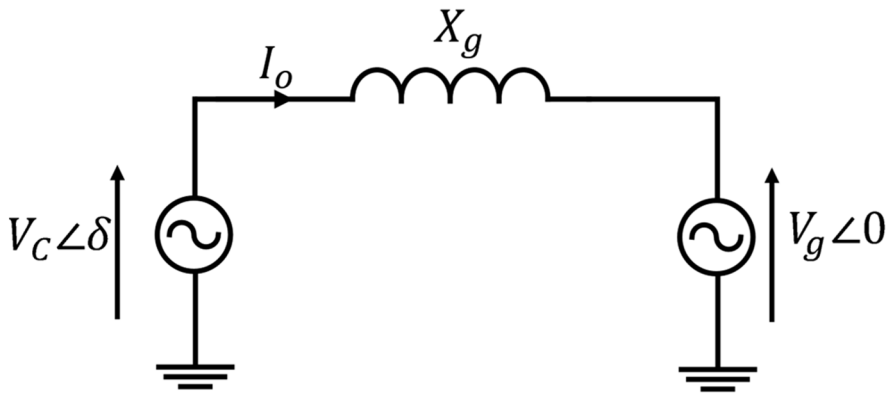

Fig. 1-3. Equivalent circuit of grid-forming inverter and grid.

The principle of the droop control is discussed here. Fig. 1-3 shows the equivalent circuit, described by phasor, of the grid-forming inverter and the grid, where δ is the phase of V_c with respect to V_g. It is assumed here that the grid is sufficiently inductive as $\omega L_g = X_g >> R_g$. The complex power S supplied from the inverter to the grid can be written as follows, where the output current of inverter is I_o.

$$
\begin{aligned}
I_o &= \frac{V_C e^{j\delta} - V_g e^{j0}}{X_g e^{j\frac{\pi}{2}}} \\
&= \frac{1}{X_g}\left(V_C e^{j\left(\delta-\frac{\pi}{2}\right)} - V_g e^{-j\frac{\pi}{2}}\right)
\end{aligned} \tag{1.1}
$$

$$
\begin{aligned}
S &= V_C^* I_o \\
&= \frac{V_C e^{-j\delta}}{X_g}\left(V_C e^{j\left(\delta-\frac{\pi}{2}\right)} - V_g e^{-j\frac{\pi}{2}}\right) \\
&= \frac{V_C V_g}{X_g}\sin\delta + j\left(\frac{V_C V_g}{X_g}\cos\delta - \frac{V_C^2}{X_g}\right)
\end{aligned} \tag{1.2}
$$

where * denotes the complex conjugate. The active power P and reactive power Q are real and imaginary parts of equation (1.2), respectively.

$$
P = \frac{V_C V_g}{X_g}\sin\delta \ , \ Q = \frac{V_C V_g}{X_g}\cos\delta - \frac{V_C^2}{X_g} \tag{1.3}
$$

Equation (1.3) can be linearized at the operating point, where δ_0 and V_{c0} are values at the operating point of δ and V_c respectively, and are described as small signal models as follows:

$$
\begin{aligned}
\Delta P &= \left.\frac{\partial P}{\partial V_C}\right|_{\substack{V_c = V_{c0} \\ \delta = \delta_0}} \Delta V_C + \left.\frac{\partial P}{\partial \delta}\right|_{\substack{V_c = V_{c0} \\ \delta = \delta_0}} \Delta\delta \\
&= \left(\frac{V_g}{X_g}\sin\delta_0\right)\Delta V_C + \left(\frac{V_{C0} V_g}{X_g}\cos\delta_0\right)\Delta\delta
\end{aligned} \tag{1.4}
$$

$$
\begin{aligned}
\Delta Q &= \left.\frac{\partial Q}{\partial V_C}\right|_{\substack{V_c = V_{c0} \\ \delta = \delta_0}} \Delta V_C + \left.\frac{\partial Q}{\partial \delta}\right|_{\substack{V_c = V_{c0} \\ \delta = \delta_0}} \Delta\delta \\
&= \left(\frac{V_g\cos\delta_0 - 2V_{C0}}{X_g}\right)\Delta V_C + \left(-\frac{V_{C0} V_g}{X_g}\sin\delta_0\right)\Delta\delta
\end{aligned} \tag{1.5}
$$

Assuming that the phase difference between the inverter voltage and the grid voltage is $\delta_0 \cong 0$, where $\sin\delta_0 \cong 0$ and $\cos\delta_0 \cong 1$, ΔP and ΔQ can be rewritten as follows:

$$\Delta P = \frac{V_{C0} V_g}{X_g} \Delta\delta \tag{1.6}$$

$$\Delta Q = \frac{V_g - 2V_{C0}}{X_g} \Delta V_C \tag{1.7}$$

Equations (1.6)and (1.7) indicate that the active power and reactive power are decoupled at the operating point i.e., the active power can be controlled by the phase of the inverter voltage, while the reactive power can be controlled by the amplitude of the inverter voltage. In other words, the phase and amplitude of the inverter voltage, which the inverter outputs in response to fluctuations in power demand, should be determined according to the equations below, where $m_p > 0$ and $n_q < 0$ are defined as P-f and Q-V droop coefficients, respectively.

$$\Delta\delta = m_p \Delta P \tag{1.8}$$

$$\Delta V_C = n_q \Delta Q \tag{1.9}$$

Equations (1.8)and (1.9) can be rewritten as shown in equations (1.10)and (1.11) by defining $\Delta P = p - p_{ref}$ and $\Delta Q = q - q_{ref}$ .As shown in Fig. 1-4, the active and reactive power can be controlled to the reference values by operating the frequency and amplitude of the inverter voltage, respectively.

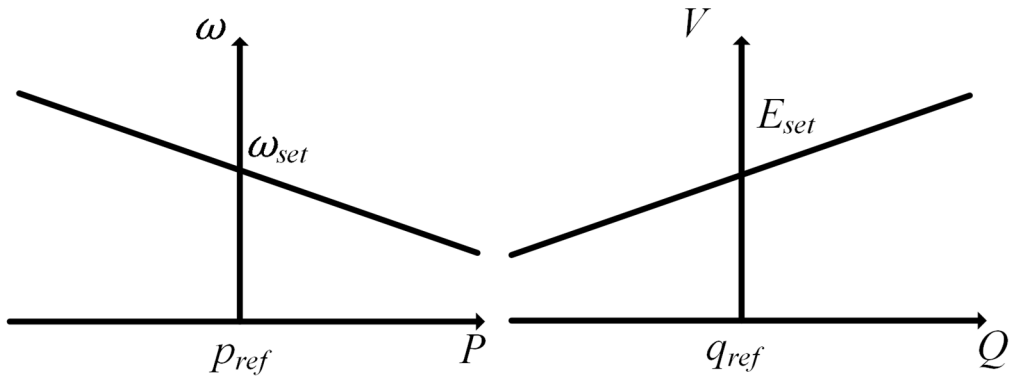

Fig. 1-4. Frequency and voltage droop characteristics in grids with dominant inductive behavior.

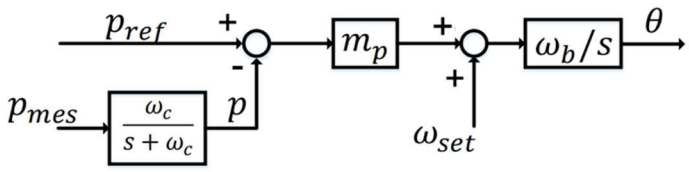

(a) P-f droop

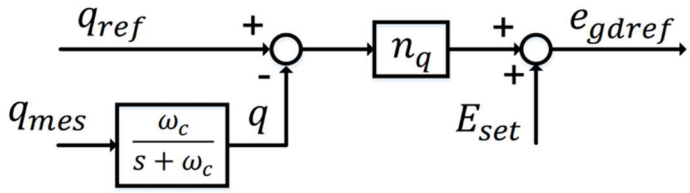

(b) Q-V droop

Fig. 1-5. Droop control.

$$\omega - \omega_{set} = -m_p\left(p - p_{ref}\right) \tag{1.10}$$

$$E - E_{set} = -n_q\left(q - q_{ref}\right) \tag{1.11}$$

The block diagrams of the conventional droop control are shown in Fig. 1-5. The measured active and reactive power are defined as p_{mes} and q_{mes}, respectively. To avoid power noises, a low-pass filter is added on the active and reactive power measurement, where ω_c is the cut-off angular frequency. This low-pass filter also provides a function of virtual inertia to the inverter, and it was proven that the droop control and VSM are mathematically identical at the operating point [25]. Fig. 1-5 indicates that when p_{ref} is smaller than p, frequency is decreased to reduce the phase difference δ. In contrast, when p_{ref} is larger than p, frequency is increased to enlarge the phase difference δ. The same is true for the reactive power.

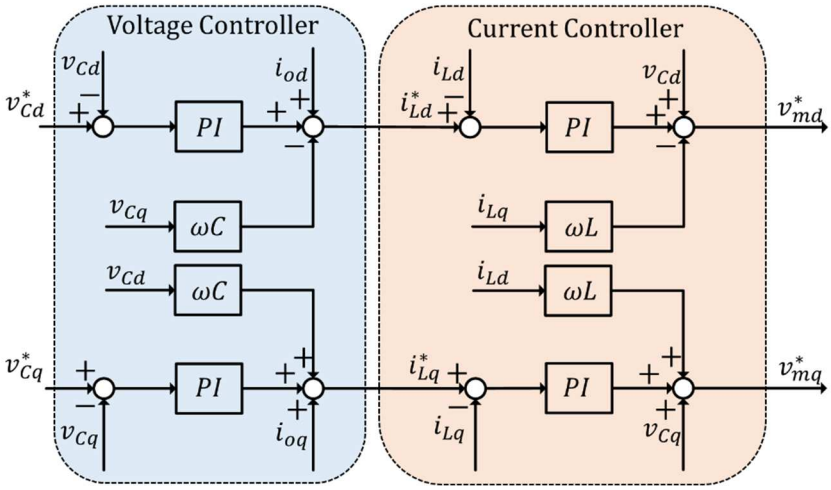

Fig. 1-6. Cascaded PI voltage control.

A cascaded PI controller in the *dq*-domain shown in Fig. 1-6 has been investigated as an inner controller for voltage regulation. The cascaded PI controller consists of an inner controller for the filter inductor current i_L and an outer controller for the capacitor voltage v_c. The outer closed loop voltage controller is composed of two PI controllers and a feedforward for decoupling the coupling $\omega C v_{dq}$ between the d-axis and the q-axis, and a compensation for the current i_{odq}. The outer voltage controller calculates the reference value of the filter inductor current i_{Ldq}. The inner current controller is the same structure as the outer voltage controller, and it outputs the reference of the inverter voltage v_{mdq}.

The advantage of the cascaded PI controller is the ability to obtain the current reference from the voltage control so that grid-forming inverters prevent overcurrent in the case of grid-fault. However, the design of the PI controllers is difficult because of the system coupling and the controller's bandwidth. Conventionally, PI controllers in cascaded structures are independently tuned in the frequency-domain by setting a faster response time for the inner loop and a slower one for the outer loops. The inner current controller gains are tuned by setting a slower response time than the PWM response described in equation (1.12), which can be described as the first-order transfer function that approximates the effect of the PWM [26].

$$G_{pwm}(s) = \frac{1}{\frac{1}{2f_{sw}}s + 1} \tag{1.12}$$

where f_{sw} is the switching frequency of the inverter. With the above conventional tuning method, it is difficult to design a control gain that stabilizes the system especially in the grid-connected mode, hence various tuning methods and control system designs have been proposed [26]-[28]. Reference literature [28], which proposed the tuning method of the voltage control gains based on the small-signal model and the participation factor,

aims to improve the response of the voltage by analyzing the eigenvalues of the entire system. In reference literature [29], robust control is enabled by applying H_2/H_∞ control to the voltage loop, and in reference literature [30], voltage control responsiveness is improved by using a fractional order controller (FOC).

1.2.3 Stability analysis

This section introduces the reason why an interaction between grid-connected inverters and the grid may destabilize the grid system, and presets the analysis methods of system stability in the literature.

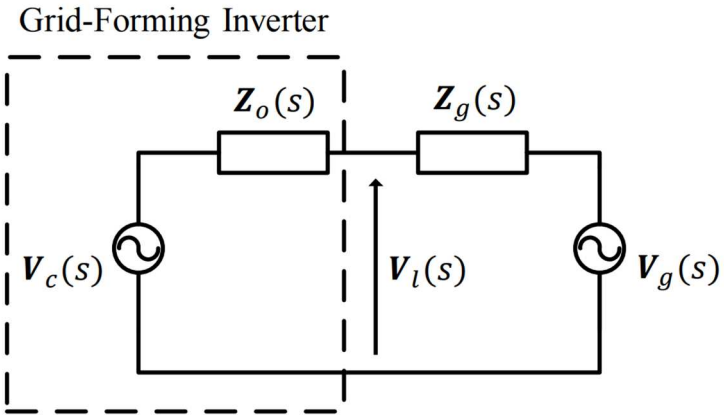

Fig. 1-7. Equivalent circuit of a grid-forming inverter and a grid.

The system in Fig. 1-2 can be modeled into two subsystems as shown in Fig. 1-7. Since the grid-forming inverter behaves as a voltage source, the inverter is expressed as the Thevenin's circuit composed of the output impedance $Z_o(s)$ and the inverter control voltage $V_c(s)$. The grid system can also be expressed with the Thevenin's circuit composed of the line impedance $Z_g(s)$ and the equivalent grid voltage $V_g(s)$. Then the interfaced voltage $V_l(s)$ can be written as equation (1.13):

$$V_l(s) = \frac{1}{1 + Z_o(s)/Z_g(s)} \left\{ V_c(s) + \left(Z_o(s)/Z_g(s) \right) V_g(s) \right\} \tag{1.13}$$

The fraction of this equation can be described by the block diagram shown in Fig. 1-8. It shows that the system has a negative feedback control system with the forward gain $Z_o(s)/Z_g(s)$. In linear control theory, the system is stable if and only if $Z_o(s)/Z_g(s)$ satisfies the Nyquist stability criterion.

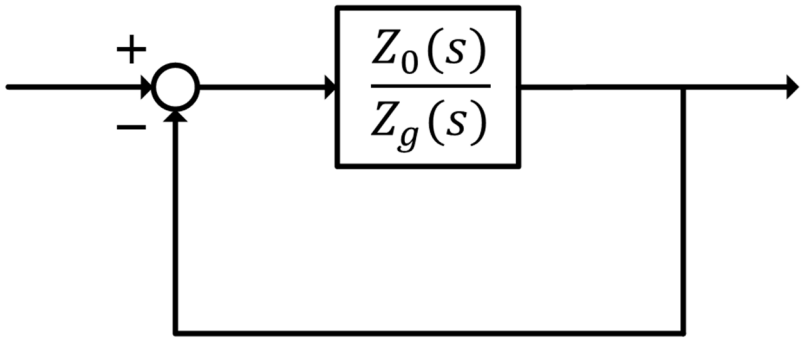

Fig. 1-8. Block diagram of the equivalent circuit.

It is also indicated that high impedance of the grid-forming inverter or low impedance of the grid may destabilize the inverter control loop and lead to sustained harmonic resonance or other instability problems.

Table 1-3. Stability analysis methods [31]

Stability analysis method	**Domain**	**Modeling**	**Measurement**
State-space analysis	Time-domain	White-box modeling	---
Impedance-based analysis [32]	Frequency-domain	Black-box modeling	Frequency scan [33]

There are two stability analysis methods as summarized in Table 1-3 [31]. The first is the state-space analysis method. The state-space model at the operating point is derived and the stability of the whole grid system, including grid-connected inverters, is analyzed by its eigenvalues. This method often requires high order system as the number of grid-connected inverters increases. Moreover, to derive a state-space model, "white-box" modeling is needed, which is an inverter model that includes control schemes and parameters that are usually confidential.

The second analysis method is the impedance-based stability criterion [32]. Applying the Nyquist criterion to the denominator of equation (1.13), the system is stable when the phase of $Z_o(s)/Z_g(s)$ is less than 180 degrees or $|Z_o(s)/Z_g(s)| < 1$ at the cross frequency of 180 degrees. It is equivalent that the phase difference of $Z_o(s)$ and $Z_g(s)$ is less than 180 degrees or $|Z_o(s)| < |Z_o(s)|$ at the cross frequency. The impedance modeling is based on the transfer function that can be measured with frequency scan [33], without any inverter control schemes or parameters.

It is also noted that when the phase of the output impedance of the grid-connected inverter is passive, or the phase variation range is within ±90 degrees, the resistive component is always positive and the impedance satisfies the impedance-based stability criterion. The passive control for the grid-following inverter has been applied to Lyapunov-based control [34] and feed-forward control [35] in the literature.

1.3 Objectives and outline of the thesis

The first objective of this Ph.D. thesis is to propose control schemes and control gain tuning methods for grid-forming inverters to enhance transient response and stability. The second objective is to analyze the stability of designed systems and derive the critical point of the stability according to the control gains.

This thesis is composed of four chapters. Chapter 1 is the Introduction. Chapter 2 develops controller design and stability analysis in the *dq*-frame[J1][J2][C1][C2][C3][C6]. Chapter 3 develops the controller design and stability analysis in the *αβ*-domain[J3][J4][C4][C5][C7][C8]. Chapter 4 concludes the thesis and provides the prospects.

1.4 List of publications related to this work

The publications related to this Ph.D. thesis are as follows:

[J1] T. Qoria, C. Li, **Ko Oue**, F. Gruson, F. Colas, and X. Guillaud: “Direct AC voltage control for grid-forming inverters”, J. Power Electron, Vol.20, No.1, pp.198–211 (2020)

[J2] A. Kaneko, **Ko Oue**, T. Kato, and K. Inoue: “General-purpose computation of frequency characteristics of power conversion system for stability analysis by the impedance method”, IEEJ Transactions on industry Applications, Vol.140, No.9, pp.685-693, (2020), (in Japanese)
兼子 晶誠・大上 皓・加藤利次・井上 馨：「インピーダンス法による電力変換システムの安定性解析のための汎用周波数特性計算法」, 電気学会論文誌 D 部門, Vol.140, No.9, pp.685-693, (2020)

[J3] **Ko Oue**, S. Yano, ,S. Sano, T. Kato, and K. Inoue: “Controller design in αβ domain for grid-forming inverters by complex vector theory”, IEEJ Transactions on industry Applications, Vol.142, No.9, pp.680-688, (2022), (in Japanese)
大上 皓・矢野 颯汰・佐野 竣哉・加藤利次・井上 馨：「複素ベクトルを用いた Grid-forming inverter の αβ 領域における制御系設計」, 電気学会論文誌 D 部門, Vol.142, No.9, pp.680-688, (2022)

[J4] **Ko Oue**, S. Yano, ,S. Sano, T. Kato, and K. Inoue: “Controller design in αβ domain for grid-forming inverters by complex vector theory”, IEEJ Transactions on industry Applications, to be published, (※ [J4] is just translated [J3] into English)

[C1] T. Qoria, C. Li, **Ko. Oue**, F.Gruson, F.Colas, X.Guillaud, G. Denis, T. Prevost : “Tuning of AC voltage-controlled VSC based linear quadratic regulation”, IRSEC18, pp. 333, (2018)

[C2] **Ko Oue**, S. Sano, T. Kato, and K. Inoue: “Stability analysis of grid-forming inverter in dq frequency domain”, IEEE 20th Workshop on Control and Modeling for Power Electronics (COMPEL) (2019)

[C3] A. Kaneko, **Ko Oue,** T. Kato, and K. Inoue : “Computation of frequency characteristics of grid inverters by general small-signal analysis method”, IEEE 20th Workshop on Control and Modeling for Power Electronics (COMPEL), Paper No. 32, (2019)

[C4] **Ko Oue**, S. Sano, T. Kato, and K. Inoue: “Discrete-time voltage controller for grid-forming inverters based on complex vector theory”, IEEE 21st Workshop on Control and Modeling for Power Electronics (COMPEL) (2020)

[C5] **Ko Oue**, S. Sano, T. Kato, and K. Inoue: “Complex power control method for grid-forming inverter in αβ-domain,” IEEE Energy Conversion Congress and Exposition (ECCE), pp. 985-991 (2021)

[C6] **Ko Oue**, T. Kato, and K. Inoue: “Frequency analysis of d-q small-signal impedance model of grid-forming inverters”, SPC of IEE Japan, SPC-19- 007 (2019) (in Japanese) 大上 皓・加藤利次・井上 馨：「系統連系インバータの d-q 小信号 インピーダンスモデルの周波数解析」, 電学産業応用部門半導体電力 変換技術委員会, No.19-007 (2019)

[C7] **Ko Oue,** S. Sano, T. Kato, and K. Inoue: “Voltage controller design for grid forming inverters by complex vector theory”, SPC of IEE Japan, SPC-21- 031 (2021) 大上 皓・佐野竣哉・加藤利次・井上 馨：「複素ベクトル理論に基 づく Grid-Forming Inverter の電圧制御系設計」, 電学産業応用部門半 導体電力変換技術委員会, No.21-031 (2021)

[C8] S. Sano, **Ko Oue**, T. Kato, and K. Inoue: “Investigations on control method for grid-forming inverter based on the complex vector theory”, SPC of IEE Japan, SPC-21-038 (2021) (in Japanese) 佐野竣哉・大上 皓・加藤利次・井上 馨：「複素ベクトル理論に基 づく Grid-Forming Inverter の制御法の検討」, 電学産業応用部門半導 体電力変換技術委員会, No.21-038 (2021)

2. Controller Design and Analysis for Grid-Forming Inverter in Rotating Frame

2.1 Controller design in rotating frame

2.1.1 System modeling in rotating frame

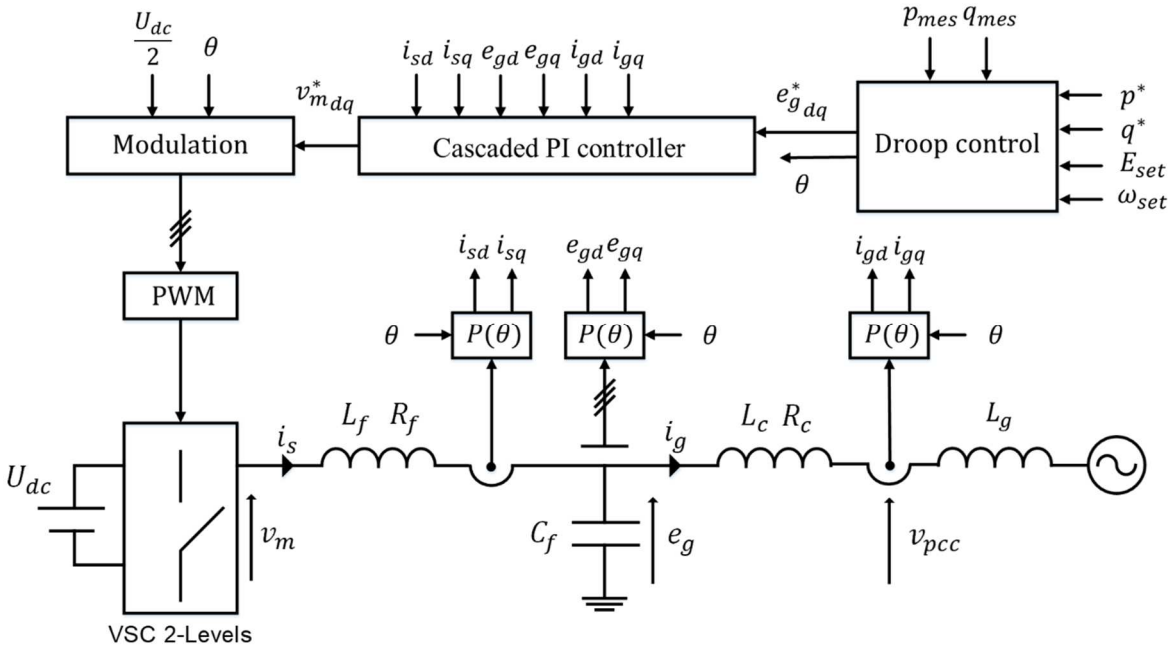

Fig. 2-1. Grid-forming inverter controlled in rotating frame.

Fig. 2-1 shows a three-phase grid-forming inverter controlled in the *dq* frame. It is connected with an AC grid through LCL filters that attenuate harmonics and is powered by an ideal DC bus. In this section, the grid is modelled as an equivalent AC voltage source and an impedance. Following the notations in Fig. 2-1, the state variables are the inverter current i_s through the filter inductor L_f in series with the resistance R_f, the voltage e_g across the filter capacitor C_f, and the current i_g through the filter inductance L_c in series with R_c and the grid inductance L_g. U_{dc}, v_{pcc}, and v_m are the ideal DC voltage, PCC voltage, and system input that is determined by a controller, respectively. The controller is composed of two control loops: an outer loop for power control that is a droop control and an inner loop that is state-feedback control for output voltage control. The system can be modeled as follows:

$$\begin{cases} \begin{bmatrix} v_{mu} \\ v_{mv} \\ v_{mw} \end{bmatrix} = \left(R_f + L_f \frac{d}{dt} \right) \begin{bmatrix} i_{su} \\ i_{sv} \\ i_{sw} \end{bmatrix} + \begin{bmatrix} e_{gu} \\ e_{gv} \\ e_{gw} \end{bmatrix} \\ C_f \frac{d}{dt} \begin{bmatrix} e_{gu} \\ e_{gv} \\ e_{gw} \end{bmatrix} = \begin{bmatrix} i_{su} \\ i_{sv} \\ i_{sw} \end{bmatrix} - \begin{bmatrix} i_{gu} \\ i_{gv} \\ i_{gw} \end{bmatrix} \\ \begin{bmatrix} e_{gu} \\ e_{gv} \\ e_{gw} \end{bmatrix} = \left(R_c + L_c \frac{d}{dt} \right) \begin{bmatrix} i_{gu} \\ i_{gv} \\ i_{gw} \end{bmatrix} + \begin{bmatrix} v_{pccu} \\ v_{pccv} \\ v_{pccw} \end{bmatrix} \end{cases} \tag{2.1}$$

Table 2-1. System parameters in SI units.

Parameter	Value	Parameter	Value
Base real power P_{base}	1 [GW]	Base voltage U_{ac}	320 [kV]
Power factor $cos\emptyset$	0.95	Resistance R_f, R_c, R_g	0.4904 [Ω]
Frequency f	50 [Hz]	Inductance L_f, L_c, L_g	0.0468 [H]
Base angular velocity ω_b	$2\pi f$ [rad/s]	Capacitance C_f	2.14 [μF]

Table 2-2. System parameters in per-unit.

Parameter	Value	Parameter	Value
P	0.5 [pu]	$R_{fpu}, R_{cpu}, R_{gpu}$	0.005 [pu]
f	50 [Hz]	$L_{fpu}, L_{cpu}, L_{gpu}$	0.15 [pu]
ω_b	$2\pi f$ [rad/s]	C_{fpu}	0.066 [pu]
m_p	0.02 [pu]	n_{qi}	-10 [pu]
E_{set}	1 [pu]	n_{qp}	0,1 [pu]
e_{gqref}	0 [pu]		

The parameters in SI unit are shown in Table 2-1. In this section, a per-unit system is used [36]. The main idea of the per-unit system is to absorb large differences in absolute values into base relationships. Thus, the representations of elements in the system with per-unit values become more uniform. The per-unit calculations are as follows:

$$S_{base} = \frac{P_{base}}{\cos \emptyset}, Z_{base} = \frac{U_{ac}^2}{S_{base}} \tag{2.2}$$

where, S_{base} and Z_{base} are base apparent power and base impedance for the per-unit system. The per-unit parameters can be calculated as below,

$$R_{fpu} = \frac{R_f}{Z_{base}}, \frac{L_{fpu}}{\omega_b} = \frac{L_f}{Z_{base}}, \frac{C_{fpu}}{\omega_b} = Z_{base} C_f \tag{2.3}$$

The parameters in the per-unit system are shown in Table 2-2.

In this section, the controller is designed in the *dq* frame. State variables in three-phase $a_{uvw} = [a_u\, a_v\, a_w]^T$ can be transformed into *dq* variables, assuming that the system is perfectly balanced so that zero phase can be negligible,

$$\begin{bmatrix} a_d \\ a_q \end{bmatrix} = \sqrt{\frac{2}{3}} \begin{bmatrix} \cos(\theta) & \cos\left(\theta - \frac{2}{3}\pi\right) & \cos\left(\theta - \frac{4}{3}\pi\right) \\ -\sin(\theta) & -\sin\left(\theta - \frac{2}{3}\pi\right) & -\sin\left(\theta - \frac{4}{3}\pi\right) \end{bmatrix} \begin{bmatrix} a_u \\ a_v \\ a_w \end{bmatrix} \tag{2.4}$$

The active and reactive power, denoted by p_{mes} and q_{mes}, respectively, are given by the following equations

$$\begin{cases} p_{mes}(t) = e_{gd}(t) i_{gd}(t) + e_{gq}(t) i_{gq}(t) \\ q_{mes}(t) = e_{gd}(t) i_{gq}(t) - e_{gq}(t) i_{gd}(t) \end{cases} \tag{2.5}$$

The state-space model of the per-unit system in the *dq* frame can be written as

$$\begin{cases} \dot{\boldsymbol{x}}_{dq}(t) = \boldsymbol{A}\boldsymbol{x}_{dq}(t) + \boldsymbol{B}\boldsymbol{u}_{dq}(t) + \boldsymbol{F}\boldsymbol{w}_{dq}(t) \\ \boldsymbol{y}_{dq}(t) = \boldsymbol{C}\boldsymbol{x}_{dq}(t) \end{cases} \tag{2.6}$$

where,

$$\begin{aligned} \boldsymbol{x}_{dq}^T &= \begin{bmatrix} i_{sd} & i_{sq} & e_{gd} & e_{gq} & i_{gd} & i_{gq} \end{bmatrix} \\ \boldsymbol{u}_{dq}^T &= \begin{bmatrix} v_{md} & v_{mq} \end{bmatrix} \\ \boldsymbol{w}_{dq}^T &= \begin{bmatrix} v_{pccd} & v_{pccq} \end{bmatrix} \end{aligned} \tag{2.7}$$

$$\boldsymbol{A}=\begin{bmatrix} -\frac{R_{fpu}\omega_b}{L_{fpu}} & \omega\omega_b & -\frac{\omega_b}{L_{fpu}} & 0 & 0 & 0 \\ -\omega\omega_b & -\frac{R_{fpu}\omega_b}{L_{fpu}} & 0 & -\frac{\omega_b}{L_{fpu}} & 0 & 0 \\ \frac{\omega_b}{C_{fpu}} & 0 & 0 & \omega\omega_b & -\frac{\omega_b}{C_{fpu}} & 0 \\ 0 & \frac{\omega_b}{C_{fpu}} & -\omega\omega_b & 0 & 0 & -\frac{\omega_b}{C_{fpu}} \\ 0 & 0 & \frac{\omega_b}{L_{cpu}} & 0 & -\frac{R_{cpu}\omega_b}{L_{cpu}} & \omega\omega_b \\ 0 & 0 & 0 & \frac{\omega_b}{L_{cpu}} & -\omega\omega_b & -\frac{R_{cpu}\omega_b}{L_{cpu}} \end{bmatrix}$$

$$\boldsymbol{B}^T=\begin{bmatrix} \frac{\omega_b}{L_{fpu}} & 0 & 0 & 0 & 0 & 0 \\ 0 & \frac{\omega_b}{L_{fpu}} & 0 & 0 & 0 & 0 \end{bmatrix}, C=\begin{bmatrix} 0 & 0 & 1 & 0 & 0 & 0 \\ 0 & 0 & 0 & 1 & 0 & 0 \end{bmatrix}$$

$$\boldsymbol{F}^T=\begin{bmatrix} 0 & 0 & 0 & 0 & -\frac{\omega_b}{L_{cpu}} & 0 \\ 0 & 0 & 0 & 0 & 0 & -\frac{\omega_b}{L_{cpu}} \end{bmatrix}$$

where T denotes transposition. $\boldsymbol{x}_{dq}(t)$ and $\boldsymbol{u}_{dq}(t)$ represent the state variables and the system inputs respectively. This system is called a multiple inputs and multiple outputs (MIMO) system since it has two inputs and two outputs. It is also called a linear parameter-varying (LPV) system since the value of the frequency ω is variable in the matrix $\boldsymbol{A}$ due to the active power changing at the PCC.

The rank of this system is first taken into account. The controllability matrix can be defined as matrix $\boldsymbol{M}$:

$$\boldsymbol{M}=\begin{bmatrix} \mathbf{B} & \mathbf{AB} & \boldsymbol{A}^2\boldsymbol{B} & \boldsymbol{A}^3\boldsymbol{B} & \boldsymbol{A}^4\boldsymbol{B} & \boldsymbol{A}^5\boldsymbol{B} \end{bmatrix} \tag{2.8}$$

The rank of the controllability matrix $\boldsymbol{M}$ is 6 orders, which is the same dimension of the matrix $\boldsymbol{A}$, so this system has controllability, indicating that capacitor voltage can be controlled.

2.1.2 Design of power control

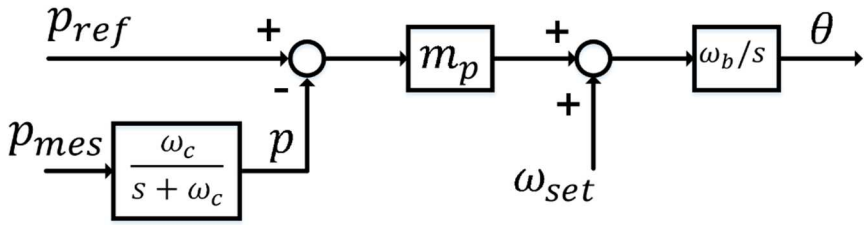

(a) P-f droop.

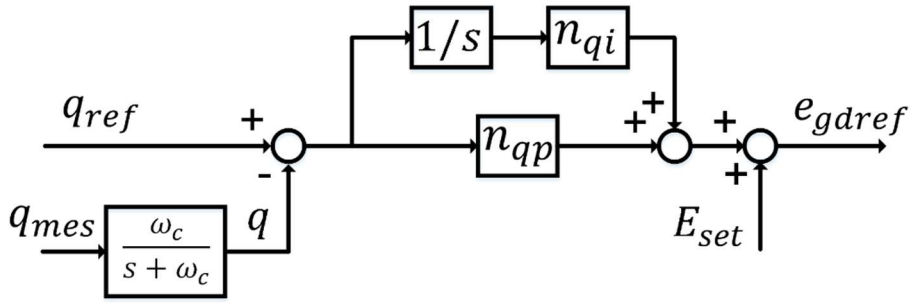

(b) Q-V droop.

Fig. 2-2. Block diagram of droop control.

Fig. 2-2 shows the block diagram of the droop control. The control is P-f and Q-V droop since the nature of the grid is sufficiently inductive as X_g>>R_g. To avoid power noises and emulate virtual inertia [21], a low-pass filter is added on the active and reactive power measurement, where ω_c is the cut-off angular frequency.

$$\begin{cases} p(s) = \dfrac{\omega_c}{s+\omega_c} p_{mes}(s) \\ q(s) = \dfrac{\omega_c}{s+\omega_c} q_{mes}(s) \end{cases} \tag{2.9}$$

For attenuating the noise of measured power, the cutoff frequency of the low pass filter is set to 31.4 rad/s (5Hz), which is 1/10 of the fundamental frequency.

The reference of the phase θ for the controlled voltage as follow:

$$\begin{cases} \omega(s) = \Delta\omega(s) + \omega_{set} \\ \Delta\omega(s) = m_p\left(p_{ref}(s) - p(s)\right) \\ \theta(s) = \dfrac{\omega_b}{s}\omega(s) \end{cases} \tag{2.10}$$

where, m_p, ω_{set}, and p_{ref} are the P-f droop gain, the fundamental frequency, and the reference of the active power, respectively. The amplitude of the controlled voltage is also determined as follows:

$$\begin{cases} \Delta E(s) = \left(n_{qp} + \dfrac{n_{qi}}{s} \right) \left(q_{ref}(s) - q(s) \right) \\ e_{gdref}(s) = E_{set} + \Delta E(s) \end{cases} \tag{2.11}$$

where n_{qp}, n_{qi}, E_{set}, and q_{ref} are the Q-V droop proportional gain, the integral gain, the fundamental amplitude of voltage, and the reference of the reactive power, respectively.

2.1.3 Design of voltage control

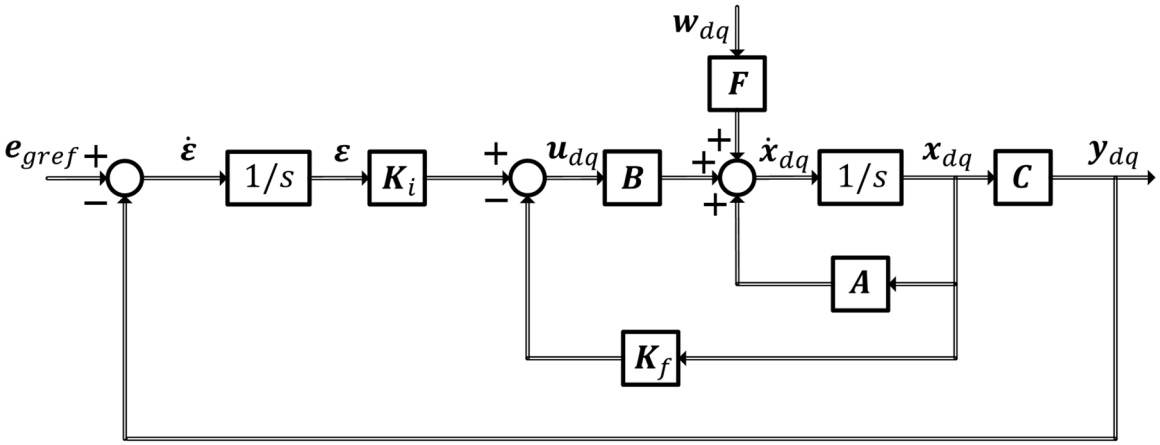

Fig. 2-3. Continuous servo-system for voltage regulation.

Grid-forming inverters are designed for autonomous operation by imposing AC voltage amplitude and frequency. This section presents a servo-system composed of a state-feedback and an integral compensator instead of the cascaded voltage and current loops. The integral compensator is sufficient to control the voltage across the capacitor without any steady-state error in the *dq* frame. Fig. 2-3 shows a block diagram of the servo system for the voltage regulation. $\boldsymbol{K_f}$ and $\boldsymbol{K_i}$ are the state- feedback gain matrix and the integral compensator matrix, respectively. The vector $\boldsymbol{e_{gref}}$ is defined as the voltage reference across the capacitor derived from the Q-V droop operation. The vector $\boldsymbol{\varepsilon}$ is the derivative of the error between the reference and the output voltage; these can be expressed in the following equations;

$$\begin{aligned} \boldsymbol{e}_{gref} &= \begin{bmatrix} e_{gdref} & e_{gqref} \end{bmatrix}^{\mathrm{T}} \\ \dot{\boldsymbol{\varepsilon}} &= \boldsymbol{e}_{gref} - \boldsymbol{y}_{dq} = \boldsymbol{e}_{gref} - \boldsymbol{C}\boldsymbol{x}_{dq} \end{aligned} \tag{2.12}$$

The controlled system of augmented matrixes can be written as

$$\begin{cases} \begin{bmatrix} \dot{\boldsymbol{x}}_{dq} \\ \dot{\boldsymbol{\varepsilon}} \end{bmatrix} = \begin{bmatrix} \boldsymbol{A} & \boldsymbol{0} \\ -\boldsymbol{C} & \boldsymbol{0} \end{bmatrix} \begin{bmatrix} \boldsymbol{x}_{dq} \\ \boldsymbol{\varepsilon} \end{bmatrix} + \begin{bmatrix} \boldsymbol{B} \\ \boldsymbol{0} \end{bmatrix} \boldsymbol{u}_{dq} + \begin{bmatrix} \boldsymbol{0} \\ \boldsymbol{I} \end{bmatrix} \boldsymbol{e}_{gref} + \begin{bmatrix} \boldsymbol{F} \\ \boldsymbol{0} \end{bmatrix} \boldsymbol{w}_{\mathbf{dq}} \\ \boldsymbol{y}_{dq} = \begin{bmatrix} \boldsymbol{C} & \boldsymbol{0} \end{bmatrix} \begin{bmatrix} \boldsymbol{x}_{dq} \\ \boldsymbol{\varepsilon} \end{bmatrix} \\ \boldsymbol{u}_{dq} = -\boldsymbol{K}_f \boldsymbol{x}_{\mathbf{dq}} + \boldsymbol{K}_i \boldsymbol{\varepsilon} = -\begin{bmatrix} \boldsymbol{K}_f & -\boldsymbol{K}_i \end{bmatrix} \begin{bmatrix} \boldsymbol{x}_{dq} \\ \boldsymbol{\varepsilon} \end{bmatrix} \end{cases} \tag{2.13}$$

In order to utilize the linear quadratic regulation (LQR), augmented matrixes are defined as

$$\begin{aligned} \tilde{\boldsymbol{x}} &= \begin{bmatrix} \boldsymbol{x}_{dq} \\ \boldsymbol{\varepsilon} \end{bmatrix} \in R^{8\times 1}, \tilde{\boldsymbol{K}} = \begin{bmatrix} \boldsymbol{K}_f & -\boldsymbol{K}_i \end{bmatrix} \in R^{2\times 8} \\ \tilde{\boldsymbol{A}} &= \begin{bmatrix} \boldsymbol{A} & \boldsymbol{0} \\ -\boldsymbol{C} & \boldsymbol{0} \end{bmatrix} \in R^{8\times 8}, \tilde{\boldsymbol{B}} = \begin{bmatrix} \boldsymbol{B} \\ \boldsymbol{0} \end{bmatrix} \in R^{8\times 2} \end{aligned} \tag{2.14}$$

This controller has 16 gains due to the controller structure, while the cascaded PI controller has only 8 gains, meaning that the proposed controller has a greater degree of freedom. Moreover, the coupling effect between the d- and q- axes can be taken into account when the gain matrices are determined.

An advantage of the quadratic optimal control method over the pole-placement method is that it provides a systematic way of computing the state-feedback control gain matrix, which is, of course, applicable to some compensator gains such as an integral compensator. Another advantage is that the designed system is always stable when matrix $\boldsymbol{P}$ exists because the LQR is based on the concept of a Lyapunov function in the progress of calculation.

The quadratic optimal regulator problem is used to determine the control gain matrix $\tilde{\boldsymbol{K}}$ so as to minimize the performance index

$$J_c = \int_0^{\infty} \left(\tilde{\boldsymbol{x}}^T \boldsymbol{Q}_c \tilde{\boldsymbol{x}} + \boldsymbol{u}_{\mathrm{dq}}^{\mathrm{T}} \boldsymbol{R}_c \boldsymbol{u}_{\mathrm{dq}} \right) \mathrm{d}t \tag{2.15}$$

where $\boldsymbol{Q}_c$ is a positive-definite (or positive-semidefinite) Hamiltonian or real symmetric matrix and $\boldsymbol{R}_c$ is a positive-definite Hamiltonian or real symmetric matrix. It is noted that the first term on the right side of the equation is related to the convergence speed of each of the state variables, and the second term accounts for the expenditure of the energy of the control signals [37].

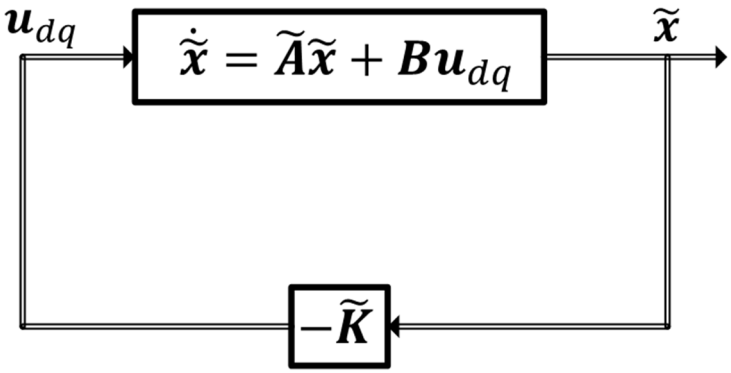

Fig. 2-4. Block diagram of the optimal regulator system.

If eigenvalues of $\tilde{A} - \tilde{B}\tilde{K}$ have all negative real parts, the system including the controller is stable, which means that the reference e_{gref} and the disturbance w_{dq} are not related to the stability. Fig. 2-4 shows the block diagram of the optimal regulator system, where the reference and the disturbance are ignored, to consider the system stability. The following equations that solves the optimization problem ignores them, substituting the system input $u_{dq} = -\tilde{K}\tilde{x}$ into the performance index equation as follows:

$$\begin{aligned} J_c &= \int_0^\infty \left(\tilde{x}^T Q_c \tilde{x} + \tilde{x}^T \tilde{K}^T R_c \tilde{K} \tilde{x} \right) \mathrm{d}t \\ &= \int_0^\infty \tilde{x}^T \left(Q_c + \tilde{K}^T R_c \tilde{K} \right) \tilde{x} \, \mathrm{d}t \end{aligned} \tag{2.16}$$

The matrix P is defined as follows;

$$\tilde{x}^T \left(Q_c + \tilde{K}^T R_c \tilde{K} \right) \tilde{x} = -\frac{d}{dt} \left(\tilde{x}^T P \tilde{x} \right) \tag{2.17}$$

where P is a positive-definite Hamiltonian or real symmetric matrix. The equation derives followings;

$$\tilde{x}^{\mathrm{T}} \left(Q_c + \tilde{K}^T R_c \tilde{K} \right) \tilde{x} = -\dot{\tilde{x}}^{\mathrm{T}} P \tilde{x} - \tilde{x}^{\mathrm{T}} P \dot{\tilde{x}} = -\tilde{x}^{\mathrm{T}} \{ (\tilde{A} - \tilde{B}\tilde{K})^{\mathrm{T}} P + P(\tilde{A} - \tilde{B}\tilde{K}) \} \tilde{x} \tag{2.18}$$

The following equation holds true for any $\tilde{x}$,

$$-\left(Q_c + \tilde{K}^T R_c \tilde{K} \right) = (\tilde{A} - \tilde{B}\tilde{K})^{\mathrm{T}} P + P(\tilde{A} - \tilde{B}\tilde{K}) \tag{2.19}$$

If $\tilde{A} - \tilde{B}\tilde{K}$ is a stable matrix, there exists a positive-definite matrix P that satisfies the equation (2.19), meaning that if it is solved and one positive-definite matrix can be P found, then the system is stable.

In order to solve the quadratic optimal problem, R_c is decomposed as follows;

$$\boldsymbol{R}_{c} = \boldsymbol{T}^{T}\boldsymbol{T} \tag{2.20}$$

where $\boldsymbol{T}$ is a nonsingular matrix. This operation is possible since $\boldsymbol{R}_c$ was set to be a positive-definite Hamiltonian or real symmetric matrix. Then equation (2.19) can be written as

$$(\tilde{\boldsymbol{A}} - \tilde{\boldsymbol{B}}\tilde{\boldsymbol{K}})^{\mathrm{T}}\boldsymbol{P} + \boldsymbol{P}(\tilde{\boldsymbol{A}} - \tilde{\boldsymbol{B}}\tilde{\boldsymbol{K}}) + \boldsymbol{Q}_{\mathrm{c}} + \tilde{\boldsymbol{K}}^{\mathrm{T}}\boldsymbol{T}^{T}\boldsymbol{T}\tilde{\boldsymbol{K}} = \boldsymbol{0} \tag{2.21}$$

which can be rewritten as

$$\tilde{\boldsymbol{A}}^{\mathrm{T}}\boldsymbol{P} + \boldsymbol{P}\tilde{\boldsymbol{A}} + \{\boldsymbol{T}\tilde{\boldsymbol{K}} - (\mathrm{T}^{\mathrm{T}})^{-1}\tilde{\boldsymbol{B}}^{\mathrm{T}}\boldsymbol{P}\}^{\mathrm{T}}\{\boldsymbol{T}\tilde{\boldsymbol{K}} - (\boldsymbol{T}^{\mathrm{T}})^{-1}\tilde{\boldsymbol{B}}^{\mathrm{T}}\boldsymbol{P}\} - \boldsymbol{P}\tilde{\boldsymbol{B}}\boldsymbol{R}_{\mathrm{c}}^{-1}\tilde{\boldsymbol{B}}^{\mathrm{T}}\boldsymbol{P} + \boldsymbol{Q}_{\mathrm{c}} = \boldsymbol{0} \tag{2.22}$$

This equation is called the Ricatti equation. To minimize the performance index J_c with the controller gain matrix $\tilde{\boldsymbol{K}}$, it should be determined as,

$$\tilde{\boldsymbol{K}} = \boldsymbol{T}^{-1}(\boldsymbol{T}^{\mathrm{T}})^{-1}\tilde{\mathrm{B}}^{\mathrm{T}}\boldsymbol{P} = \boldsymbol{R}_{\mathrm{c}}^{-1}\tilde{\boldsymbol{B}}^{T}\boldsymbol{P} \tag{2.23}$$

The matrix $\boldsymbol{P}$ in the above equation must satisfy the following reduced equation,

$$\tilde{\boldsymbol{A}}^{\mathrm{T}}\boldsymbol{P} + \boldsymbol{P}\tilde{\boldsymbol{A}} - \boldsymbol{P}\tilde{\boldsymbol{B}}\boldsymbol{R}_{\mathrm{c}}^{-1}\tilde{\boldsymbol{B}}^{\mathrm{T}}\boldsymbol{P} + \boldsymbol{Q}_{\mathrm{c}} = \boldsymbol{0} \tag{2.24}$$

This equation is called the reduced Ricatti equation.

The servo system for voltage regulation is determined for the matrices $\boldsymbol{Q}_c$ and $\boldsymbol{R}_c$ values in the equations above. However, the phase of the grid-voltage and the droop control that is non-linear should be taken into account for the parameter determination. Moreover, the feedback gains should be tuned carefully to decouple the active power control from the reactive power control, which is related to the voltage regulation. To consider the whole system behaviors, the eigenvalues of the system are analyzed using a small-signal state-space model around an operating point [38]. The derived small-signal model of the grid-forming inverter with the LQR is as follows:

$$\Delta \dot{\boldsymbol{x}}_l(t) = \boldsymbol{A}_l \Delta \boldsymbol{x}_l(t) + \boldsymbol{B}_l \Delta \boldsymbol{u}_l(t) + \boldsymbol{F}_l \Delta \boldsymbol{w}_l(t) \tag{2.25}$$

where

$$\begin{aligned}
\Delta \boldsymbol{x}_l^T &= \begin{bmatrix} \Delta\theta_s & \Delta p & \Delta q & \Delta i_{sd} & \Delta i_{sq} & \Delta e_{gd} & \Delta e_{gq} & \Delta i_{gd} & \Delta i_{gq} & \Delta\varepsilon_d & \Delta\varepsilon_q & \Delta\varsigma_q \end{bmatrix} \\
\Delta \boldsymbol{u}_l^T &= \begin{bmatrix} \Delta p_{ref} & \Delta q_{ref} & \Delta\omega_{set} & \Delta E_{set} \end{bmatrix} \\
\Delta \boldsymbol{w}_l^T &= \begin{bmatrix} \Delta v_{gd} & \Delta v_{gq} \end{bmatrix}
\end{aligned} \tag{2.26}$$

$$\Delta \boldsymbol{A}_l = \begin{bmatrix}
0 & -m_p\omega_b & 0 & 0 & 0 & 0 & 0 & 0 & 0 & 0 & 0 & 0 \\
0 & -\omega_c & 0 & 0 & 0 & \omega_c I_{gd} & \omega_c I_{gq} & \omega_c E_{gd} & \omega_c E_{gq} & 0 & 0 & 0 \\
0 & 0 & -\omega_c & 0 & 0 & \omega_c I_{gq} & -\omega_c I_{gd} & -\omega_c E_{gq} & \omega_c E_{gd} & 0 & 0 & 0 \\
0 & 0 & 0 & -\dfrac{\omega_b(R_{fpu}+k_{f11})}{L_{fpu}} & \omega\omega_b - \dfrac{\omega_b k_{f12}}{L_{fpu}} & -\dfrac{\omega_b(1+k_{f13})}{L_{fpu}} & -\dfrac{\omega_b k_{f14}}{L_{fpu}} & -\dfrac{\omega_b k_{f15}}{L_{fpu}} & -\dfrac{\omega_b k_{f16}}{L_{fpu}} & \dfrac{\omega_b k_{i11}}{L_{fpu}} & \dfrac{\omega_b k_{i12}}{L_{fpu}} & 0 \\
0 & 0 & 0 & -\omega\omega_b - \dfrac{\omega_b k_{f21}}{L_{fpu}} & -\dfrac{\omega_b(R_{fpu}+k_{f22})}{L_{fpu}} & -\dfrac{\omega_b k_{f23}}{L_{fpu}} & -\dfrac{\omega_b(1+k_{f24})}{L_{fpu}} & -\dfrac{\omega_b k_{f25}}{L_{fpu}} & -\dfrac{\omega_b k_{f26}}{L_{fpu}} & \dfrac{\omega_b k_{i12}}{L_{fpu}} & \dfrac{\omega_b k_{i22}}{L_{fpu}} & 0 \\
0 & 0 & 0 & \dfrac{\omega_b}{C_{fpu}} & 0 & 0 & \omega\omega_b & -\dfrac{\omega_b}{C_{fpu}} & 0 & 0 & 0 & 0 \\
0 & 0 & 0 & 0 & \dfrac{\omega_b}{C_{fpu}} & -\omega\omega_b & 0 & 0 & -\dfrac{\omega_b}{C_{fpu}} & 0 & 0 & 0 \\
\dfrac{\omega_b(V_{gd}\sin\theta_s - V_{gq}\cos\theta_s)}{L_{cpu}} & 0 & 0 & 0 & 0 & \dfrac{\omega_b}{L_{cpu}} & 0 & -\dfrac{\omega_b R_{cpu}}{L_{cpu}} & \omega\omega_b & 0 & 0 & 0 \\
\dfrac{\omega_b(V_{gd}\cos\theta_s + V_{gq}\sin\theta_s)}{L_{cpu}} & 0 & 0 & 0 & 0 & 0 & \dfrac{\omega_b}{L_{cpu}} & -\omega\omega_b & -\dfrac{\omega_b R_{cpu}}{L_{cpu}} & 0 & 0 & 0 \\
0 & 0 & -n_{qp} & 0 & 0 & -1 & 0 & 0 & 0 & 0 & 0 & n_{qi} \\
0 & 0 & 0 & 0 & 0 & 0 & -1 & 0 & 0 & 0 & 0 & 0 \\
0 & 0 & -1 & 0 & 0 & 0 & 0 & 0 & 0 & 0 & 0 & 0
\end{bmatrix} \tag{2.27}$$

$$\Delta \boldsymbol{B}_l = \begin{bmatrix} m_p\omega_b & 0 & \omega_b & 0 \\ 0 & 0 & 0 & 0 \\ 0 & 0 & 0 & 0 \\ 0 & 0 & 0 & 0 \\ 0 & 0 & 0 & 0 \\ 0 & 0 & 0 & 0 \\ 0 & 0 & 0 & 0 \\ 0 & 0 & 0 & 0 \\ 0 & 0 & 0 & 0 \\ 0 & 0 & 0 & 1 \\ 0 & 0 & 0 & 0 \\ 0 & 1 & 0 & 0 \end{bmatrix}, \Delta \boldsymbol{F}_l = \begin{bmatrix} 0 & 0 \\ 0 & 0 \\ 0 & 0 \\ 0 & 0 \\ 0 & 0 \\ 0 & 0 \\ 0 & 0 \\ -\frac{\omega_b \cos\theta_s}{L_{cpu}} & -\frac{\omega_b \sin\theta_s}{L_{cpu}} \\ \frac{\omega_b \sin\theta_s}{L_{cpu}} & -\frac{\omega_b \cos\theta_s}{L_{cpu}} \\ 0 & 0 \\ 0 & 0 \\ 0 & 0 \end{bmatrix} \tag{2.28}$$

The operating point are listed in Table 2-3. E_{gd}, E_{gq}, I_{gd}, I_{gq}, V_{gd}, and V_{gq} are the values at the operating point of e_{gd}, e_{gq}, i_{gd}, i_{gq}, and grid-voltage on the dq-frame respectively. θ_s, which is defined as a phase difference between the capacitor voltage and the grid voltage, can be converted to a constant value under steady-state conditions. Table 2-4 shows the eigenvalues of the state transition matrix $\boldsymbol{A}_l$ when both weighting matrices $\boldsymbol{Q}_c$ and $\boldsymbol{R}_c$ identity matrices. The three eigenvalues, $\lambda_{10\text{-}11}$ and λ_{12} indicate that the stability margin of this system is relatively small since they are close to the imaginary axis. The controller gains should be tuned to acquire a better stability margin.

Table 2-3. Operating point.

Operating point	Values	Operating point	Values
θ_s	0.316 [rad]	I_{gd}	0.5 [pu]
$\cos\theta_s$	0.95	I_{gq}	0 [pu]
$\sin\theta_s$	0.3123	V_{gd}	1 [pu]
E_{gd}	1 [pu]	V_{gq}	0 [pu]
E_{gq}	0 [pu]		

Table 2-4. System eigenvalues with $\boldsymbol{Q}_c$ and $\boldsymbol{R}_c$ identity matrices.

$\lambda_{1\text{-}2}$= -1337 $\pm$ 4519j	$\lambda_{3\text{-}4}$= -1337 $\pm$ 3891j
$\lambda_{5\text{-}6}$= -1137 $\pm$ 3891j	λ_7= -31
$\lambda_{8\text{-}9}$= -13 $\pm$ 10j	$\lambda_{10\text{-}11}$= -0.416 $\pm$ 3.42j
λ_{12}= -2.76	

Table 2-5. LQR weight.

Q_1~ Q_6 = 1	Q_7 , Q_8 = 10^7	R_1 , R_2 = 1

Table 2-6. System eigenvalues after tuning.

$\lambda_{1\text{-}2}$= -1458 ± 4658j	$\lambda_{3\text{-}4}$= -1375 ± 4075j
$\lambda_{5\text{-}6}$= -1802 ± 145j	$\lambda_{7\text{-}8}$= -162 ± 207j
$\lambda_{9\text{-}10}$= -14 ± 27j	$\lambda_{11\text{-}12}$= -5.19 ± 39.1j

The participation factor is utilized to tune the controller gains. The participation factor shows a sensitivity of an eigenvalue to a state variable [39]. The participation factor of mode k to a state variable j is defined as

$$\rho = \boldsymbol{q}_{kj}^{T} \boldsymbol{p}_{kj} \tag{2.29}$$

where $\boldsymbol{q}_{kj}$ and $\boldsymbol{p}_{kj}$ are the j-th components of the left and right eigenvectors of mode k for the linearized matrix $\boldsymbol{A}_l$. The participation factors for eigenvalues $\lambda_{10\text{-}11}$ and λ_{12}, presented in Fig. 2-5 and Fig. 2-6, show the link with ε_d and ε_q, respectively. This indicates that the weighting factor Q_7 and Q_8 should be increased in order to improve the voltage dynamics. The weighting matrices are finally determined as shown in Table 2-5 and the eigenvalues are shown in Table 2-6. The system has more stability margins rather than just the one before tuning.

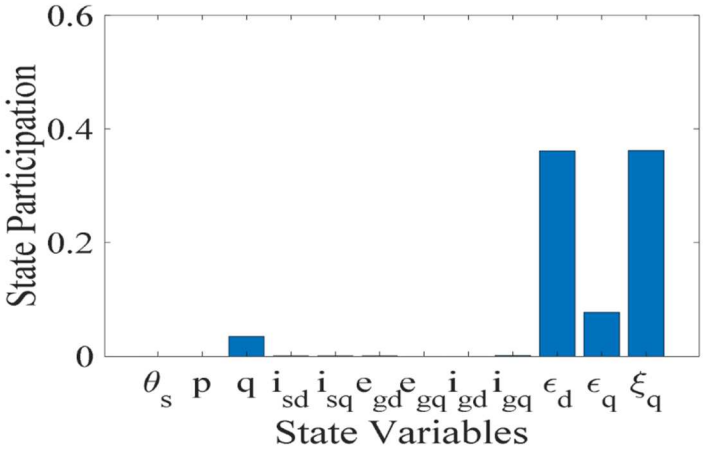

Fig. 2-5. State variables participation on $\lambda_{10\text{-}11}$.

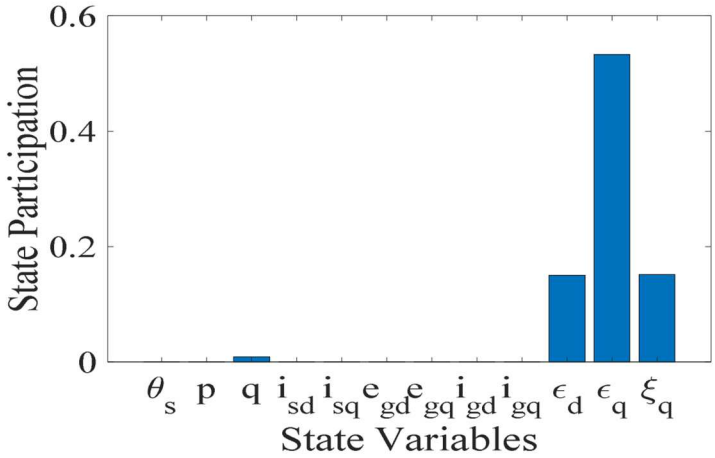

Fig. 2-6. State variables participation on λ_{12}.

In order to investigate the proposed control, the cascaded PI [28] and the proposed controls are compared by MATLAB/Simulink. The voltage step response is applied to the system E_{set} = 1.1 pu at t = 0.1 sec. This case was chosen in order to check the coupling between the active power and controlled voltage. The results are shown in Fig. 2-7. The proposed method generates a faster response with much smaller overshoot compared to the cascaded PI controller. The proposed method also presents a very small transient coupling effect between the active and reactive powers (voltage), in contrast to the cascaded PI controller.

The active power response is also applied to the system shown in Fig. 2-8. Thanks for the well-tuned control gains, the proposed method has lower overshoot of the active power and less coupling to the voltage than the conventional one.

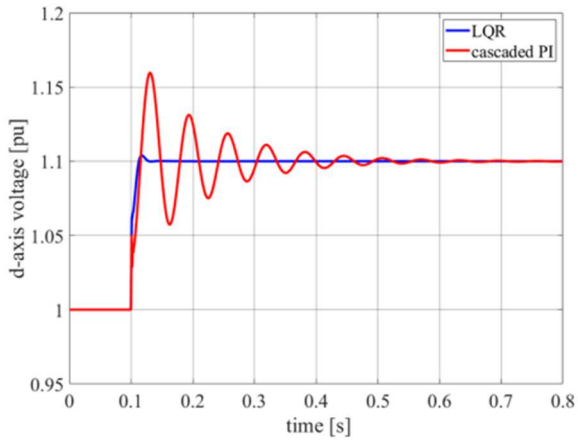

(a) d-axis voltage

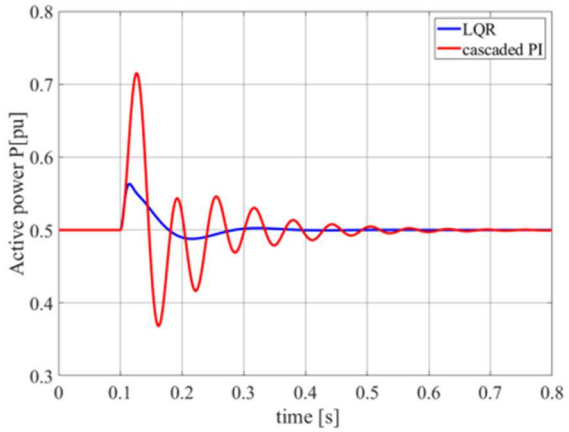

(b) Active power

Fig. 2-7. Proposed control performance compared to cascaded PI (Voltage step response).

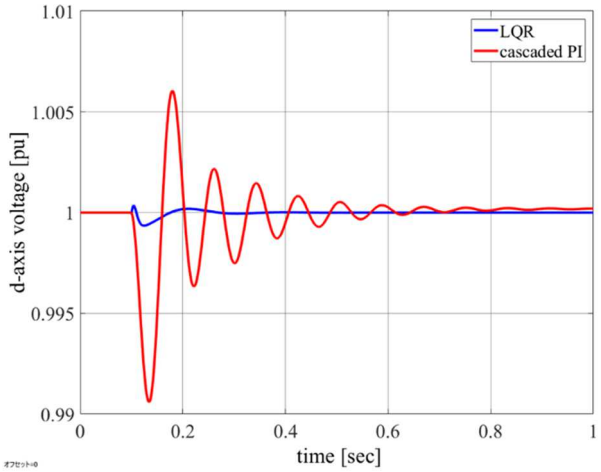

(a) d-axis voltage

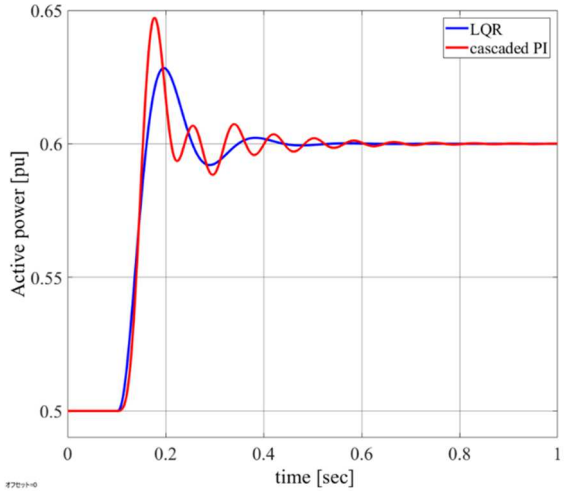

(a) Active power

Fig. 2-8. Proposed control performance compared to cascaded PI (Active power step response).

2.2 Impedance and stability analysis in rotating frame

Due to interactions among grid-connected inverters, the grid system might possibly become unstable. To analyze the stability of the circuit system including the grid-connected inverters, the impedance-based stability criterion is widely applied [32]. In this section, the stability based on the impedance method and the eigenvalue analysis is investigated and validated by numerical simulations, and the stability of the LQR is compared to the cascaded PI controller.

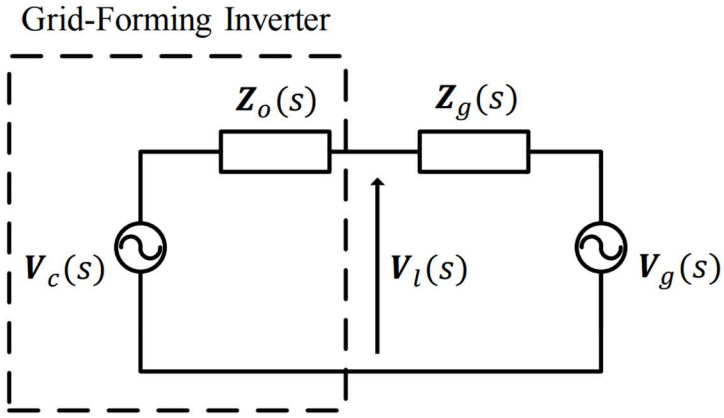

Fig. 2-9. Small-signal equivalent circuit of a three-phase grid system in the *dq* frame.

The stability is analyzed by the impedance-based small-signal method in the *dq* frame. The linearization of the nonlinear circuit around the operating point is needed for deriving the small-signal impedance of the grid-connected inverter. The system in Fig. 2-1 can be modeled into two subsystems as shown in Fig. 2-9. Since the grid-forming inverter behaves as a voltage source, the inverter is expressed as the Thevenin's circuit composed of the output impedance 2×2 matrix $\boldsymbol{Z_o}(s)$ and the inverter control voltage $\boldsymbol{V_c}(s)$. The grid system can also be expressed with the Thevenin's circuit composed of the line impedance 2×2 matrix $\boldsymbol{Z_g}(s)$ and the equivalent grid voltage $\boldsymbol{V_g}(s)$. Then the interfaced voltage $\boldsymbol{V_l}(s)$ can be written as equation (2.30) and the minor loop $\boldsymbol{L}(s)$ can be defined as equation (2.31).

$$\boldsymbol{V}_l(s) = \boldsymbol{V}_c(s) - \boldsymbol{Z}_o(s)\left(\boldsymbol{I} + \boldsymbol{Z}_o(s)\boldsymbol{Z}_g^{-1}(s)\right)^{-1}\boldsymbol{Z}_g(s)\left(\boldsymbol{V}_c(s) - \boldsymbol{V}_g(s)\right) \tag{2.30}$$

$$\boldsymbol{L}(s) = \boldsymbol{Z}_o(s)\boldsymbol{Z}_g^{-1}(s) \tag{2.31}$$

where, $\boldsymbol{I}$ is the identity matrix. Applying the generalized Nyquist criterion to the minor loop $\boldsymbol{L}(s)$, the system is stable if the eigenloci of the $\boldsymbol{L}(s)$ encircle is greater than the -1, or crosses to the right side, when the phase is 180° [40]. It is noted that the eigenloci is the loci of the eigenvalues of the loop gain transfer function matrix parameterized as a function of frequency.

In the frequency-domain, the output impedance of the grid-forming inverter can be derived from equation (2.30);

$$\begin{aligned}\left[\begin{array}{cc}\Delta I_{gd}(s) & \Delta I_{gq}(s)\end{array}\right]^{T} &= \boldsymbol{C}_{l}\Delta \boldsymbol{X}(s) \\ &= \boldsymbol{C}_{l}\left(s\boldsymbol{I}-\boldsymbol{A}_{l}\right)^{-1}\boldsymbol{B}_{l}\Delta \boldsymbol{U}_{l}(s)+\boldsymbol{C}_{l}\left(s\boldsymbol{I}-\boldsymbol{A}_{l}\right)^{-1}\boldsymbol{F}_{l}\Delta \boldsymbol{W}_{l}(s)\end{aligned} \tag{2.32}$$

The second term on the right side represents the transfer function from the grid-voltage to the injected currents to the grid, and is equivalent to output admittance. The output admittance $\boldsymbol{Y_o}(s)$ can be written as

$$\boldsymbol{Y}_{o}(s)=\left[\begin{array}{cc}\boldsymbol{Y}_{odd}(s) & \boldsymbol{Y}_{odq}(s) \\ \boldsymbol{Y}_{oqd}(s) & \boldsymbol{Y}_{oqq}(s)\end{array}\right]=-\left\{\boldsymbol{C}_{l}\left(sI-\boldsymbol{A}_{l}\right)^{-1}\boldsymbol{F}_{1}\right\}^{-1} \tag{2.33}$$

Considering the direction of the defined current, the negative sign should be added. The output impedance where the system parameter is based on Table 2-2 is shown in Fig. 2-10. In order to keep the voltage constant under fluctuations of the output current, the output impedance around 0 Hz in the *dq* frame, which is around 50 Hz in the stationary frame, is designed as small as possible.

The line impedance $\boldsymbol{Z_g}(s)$ can also be written as,

$$\boldsymbol{Z}_{g}(s)=\left[\begin{array}{cc}R_{gpu}+s\dfrac{L_{gpu}}{\omega_{b}} & -\omega L_{gpu} \\ \omega L_{gpu} & R_{gpu}+s\dfrac{L_{gpu}}{\omega_{b}}\end{array}\right] \tag{2.34}$$

The stability is checked for different *P-f* droop control gain m_p. Fig. 2-11 shows the frequency characteristics of the eigenloci of the minor loop $\boldsymbol{L}(s)$. In the case of m_p = 0.21, the magnitude is -0.079 dB at 180°, indicating that this is the critical point of the stability, whereas it is unstable, when m_p = 0.22, since the magnitude of the eigenvalue is 3.51 dB which exceeds 0 dB at 180°. It can also be said that an increase in the power control gain causes enlarged output impedance gains at low frequency.

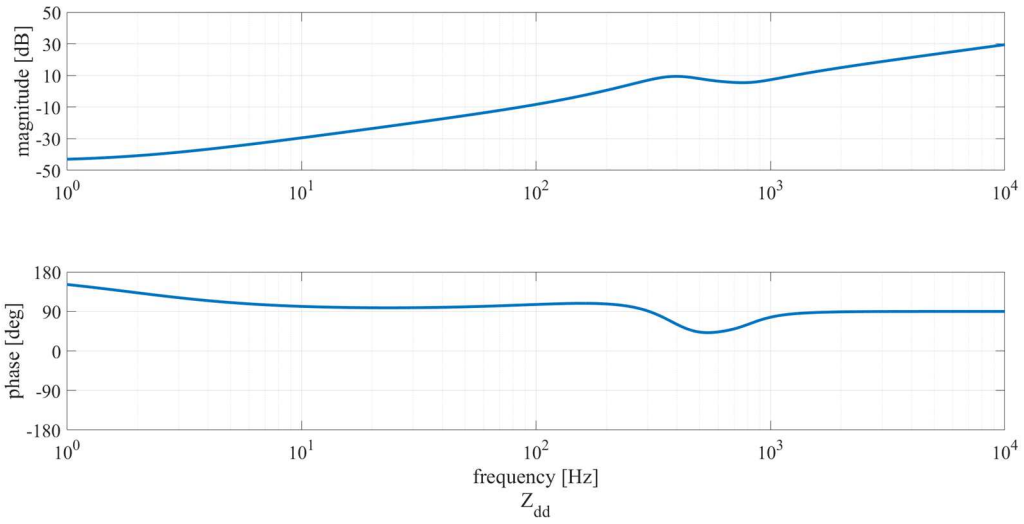
magnitude [dB]
50
30
10
-10
-30
-50
10^0
10^1
10^2
10^3
10^4
phase [deg]
180
90
0
-90
-180
frequency [Hz]
Z_{dd}

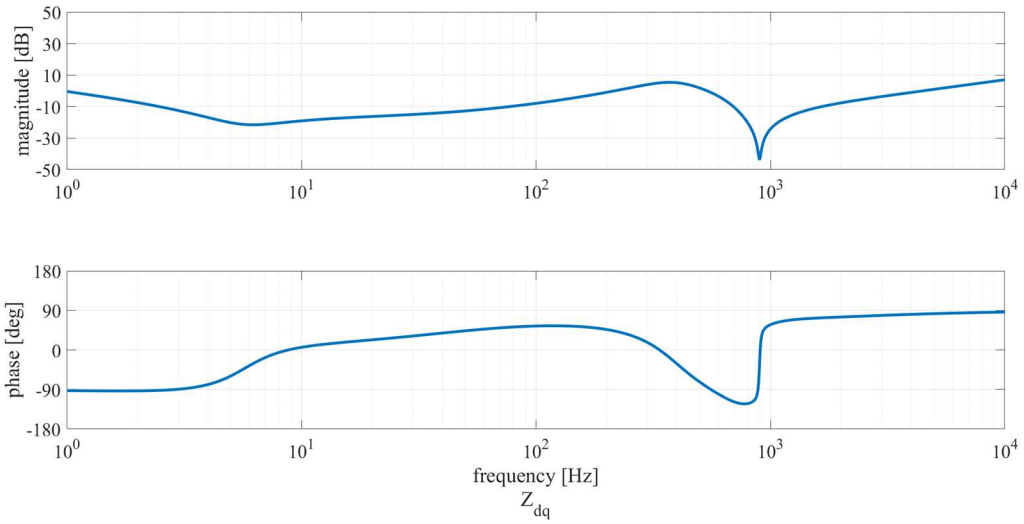
magnitude [dB]
50
30
10
-10
-30
-50
10^0
10^1
10^2
10^3
10^4
phase [deg]
180
90
0
-90
-180
frequency [Hz]
Z_{dq}

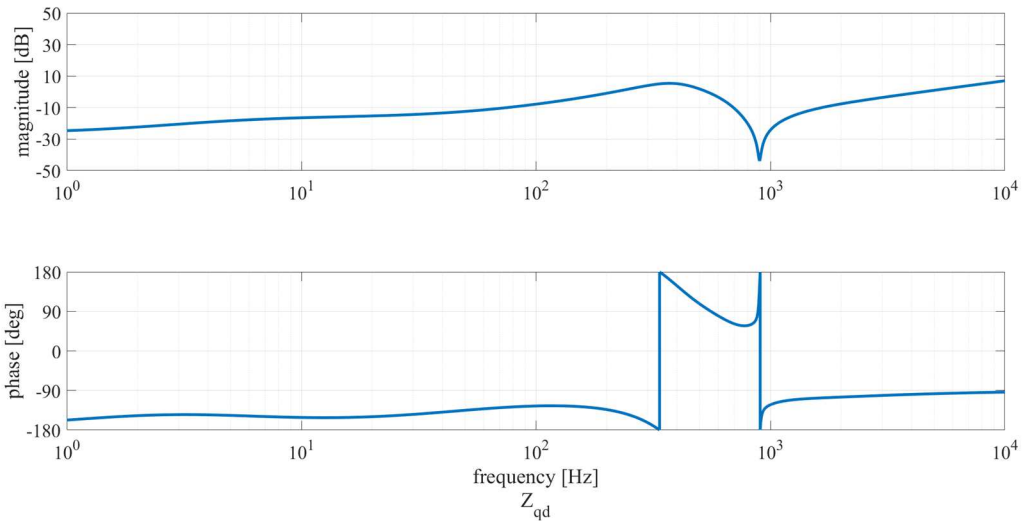
magnitude [dB]
50
30
10
-10
-30
-50
10^0
10^1
10^2
10^3
10^4
phase [deg]
180
90
0
-90
-180
frequency [Hz]
Z_{qd}

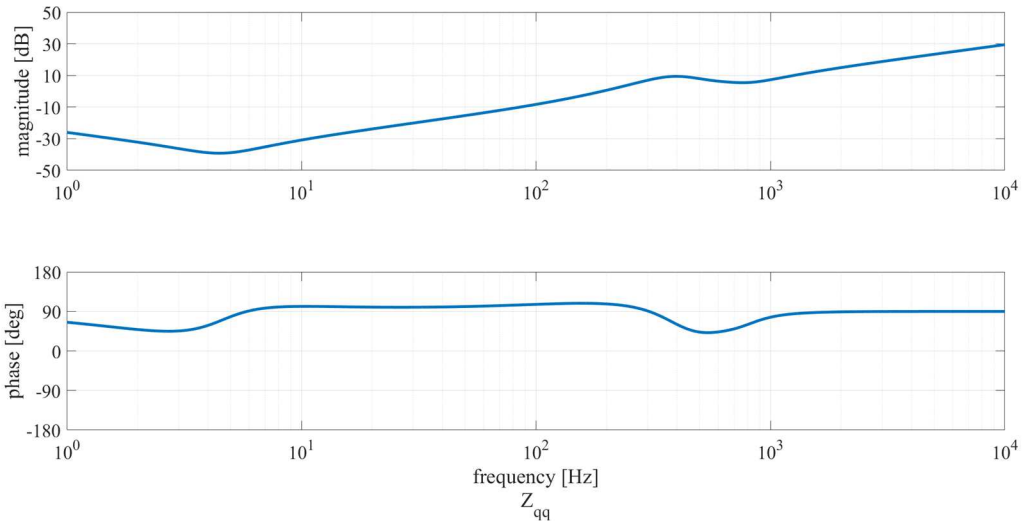

Fig. 2-10. Output impedance of grid-forming inverter.

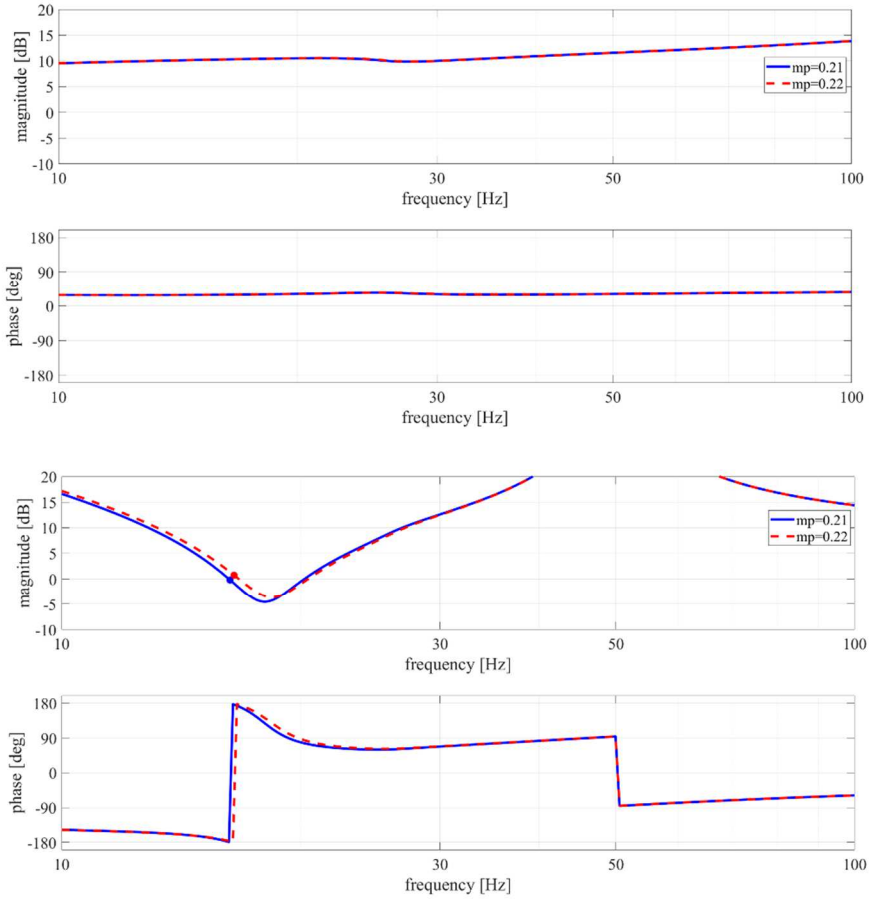

Fig. 2-11. Bode diagram of the eigen-loci of minor loop transfer function matrix $\boldsymbol{L}(s)$.

Table 2-7. Eigenvalues of $\boldsymbol{A}_l$ where $m_p = 0.20$.

$\lambda_{1\text{-}2}$= -1458 ± 4658j	$\lambda_{3\text{-}4}$= -1475 ± 146j
$\lambda_{5\text{-}6}$= -1802 ± 146j	$\lambda_{7\text{-}8}$= -176 ± 194j
$\lambda_{9\text{-}10}$= -0.3 ± 100j	$\lambda_{11\text{-}12}$= -0.570 ± 38j

Table 2-8. Eigenvalues of $\boldsymbol{A}_l$ where $m_p = 0.22$.

$\lambda_{1\text{-}2}$= -1458 ± 4658j	$\lambda_{3\text{-}4}$= -475 ± 4075j
$\lambda_{5\text{-}6}$= -1802 ± 146j	$\lambda_{7\text{-}8}$= -180 ± 191j
$\lambda_{9\text{-}10}$= 3.96 ± 112j	$\lambda_{11\text{-}12}$= -5.57 ± 38j

The stability is also investigated by the eigenvalue analysis of the linearized matrix $\boldsymbol{A}_l$, where R_{cpu} and L_{cpu} are replaced by $R_{cpu} + R_{gpu}$ and $L_{cpu} + L_{gpu}$, respectively to take the grid impedance into account. Table 2-7 and Table 2-8 show the eigenvalues of $\boldsymbol{A}_l$ where the *P-f* droop control gain m_p is 0.21 and 0.22 respectively. The eigenvalues in Table 2-7 indicate that the system is stable, whereas the positive eigenvalues $\lambda_{9\text{-}10}$ in Table 2-8 indicate that the system is unstable. Although the two stability methods are mathematically identical, and in other cases, for example, inverters are connected in parallel, the eigenvalue analysis needs considerable calculation due to the increase of the state variables. Moreover, since very few companies disclose their inverter controls and parameters, the impedance method is effective because the output impedance can be derived with black-box testing.

These stability analyses are also validated by time domain simulations with MATLAB/Simulink. The active power step response is applied to the system $p_{ref} = 0.51$ pu at $t = 1$ sec. Fig. 2-12(a) shows that the active power is converged and the system is stable where the droop coefficient $m_p = 0.21$, whereas the active power is diverged where $m_p = 0.22$ in Fig. 2-12(b). The stability analysis based on the impedance method and eigenvalues are validated with the time domain simulations.

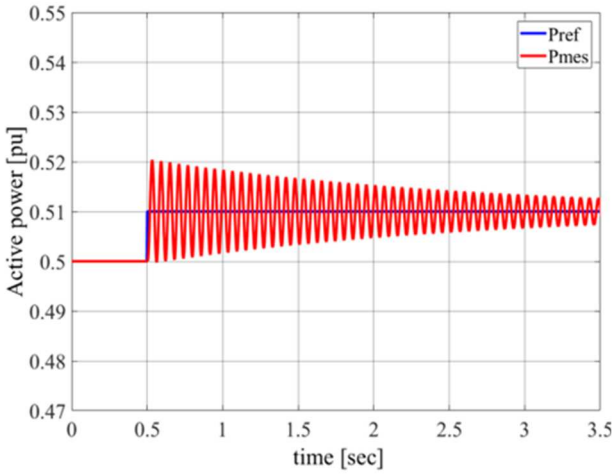

(a) m_p= 0.21

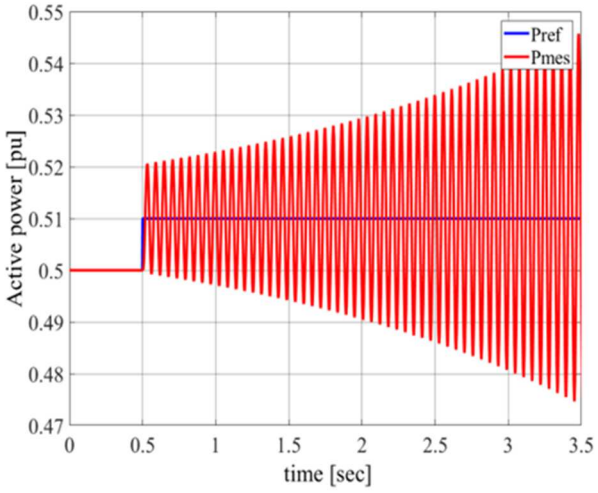

(b) m_p= 0.22

Fig. 2-12. Simulated active power of grid-forming inverter.

The output impedance of the grid-forming inverter with the cascaded PI controller can be derived the same way as in equation (2.25). The comparison of stability margins between the LQR and the cascaded PI controllers is shown in Fig. 2-13. In this case, the stability margin is considered with the power control gain m_p fixed as 0.02. Fig. 2-13 indicates clearly that the LQR has more stability margins than the cascaded PI controller.

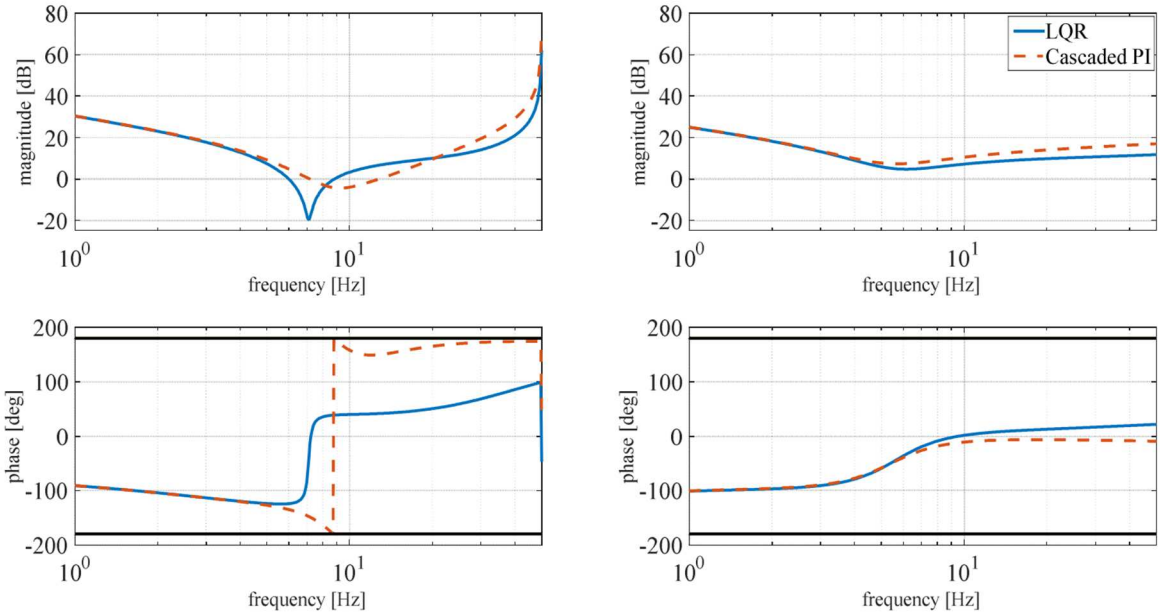

Fig. 2-13. Comparison of the stability margins between LQR and cascaded PI controllers.

2.3 Summary

This section proposes a new control method for the grid-forming inverters and analyzes the stability, which can be summarized in the following six parts.

(1) The proposed voltage controller is composed of the state-feedback and the integral compensator. The proposed controller has 16 control gains compared to the 8 gains of the cascaded PI controller; as such the former has a greater degree of freedom.

(2) Controller gains are tuned based on the LQR and the participation factor. The participation factor helps in the determination of LQR weights since it indicates the sensitivity of an eigenvalue to a state variable.

(3) Compared to the cascaded PI controller, the proposed system generates a faster voltage response with a lower overshoot and a very small transient coupling effect between the active and reactive powers.

(4) The stability is analyzed based on the impedance small-signal method in the *dq*-frame. The output impedance $\boldsymbol{Z_o}(s)$ can be derived from the small-signal state space model and the generalized Nyquist criterion is applied to the minor loop transfer function $\boldsymbol{L}(s)$ to analyze the stability.

(5) The impedance method and the eigenvalue analysis obtain the same results since they are mathematically identical. These stability analyses are also validated by time domain simulations.

(6) The LQR has better performances and more stability margins than the cascaded PI controller, which indicates that the LQR has potential to be applied to grid-forming inverters.

3. Design and Analysis of Stationary Reference Frame Controller for Grid-Forming Inverter

3.1 Design of stationary reference frame controller

3.1.1 Stationary reference frame modeling

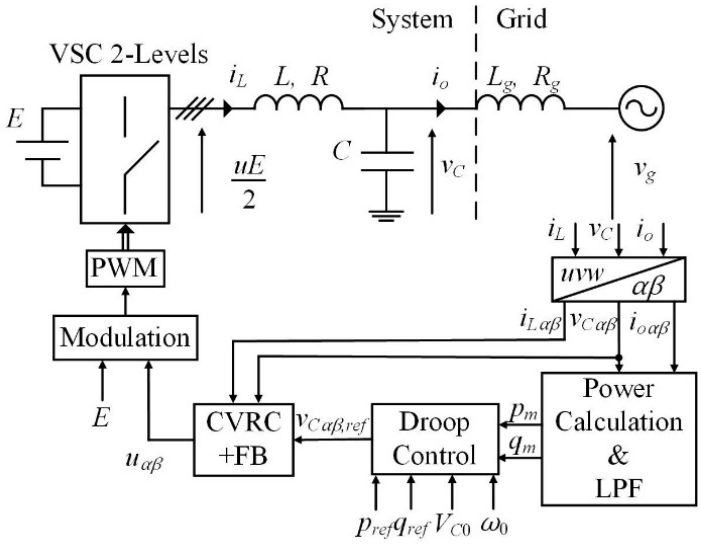

Fig. 3-1. Grid-forming inverter controlled in stationary reference frame.

Fig. 3-1. shows a three-phase grid-forming inverter controlled in a stationary reference frame. It is powered by an ideal DC bus and connected with an AC grid through LC filters that attenuate harmonics. In this section, the grid is modelled as an equivalent AC voltage source. Following the notations in Fig. 3-1, the state variables are the inverter current i_L through the filter inductor L in series with the resistance R, the voltage v_c across the filter capacitor C, and the current i_o through the grid inductance L_g in series with R_g. E, v_g, and u are the ideal DC voltage, the grid voltage, and the system input that is determined by a digital controller, respectively. The digital controller is composed of two control loops: an outer loop for power control that is a complex droop control and an inner loop that is composed of Complex Vector Resonance Controller (CVRC) and a state-feedback controller for output voltage control.

State variables in three-phase $a_{uvw} = [a_u\, a_v\, a_w]^{\mathrm{T}}$ can be transformed into the state variable denoted by the complex vector in the $\alpha\beta$-frame as

$$\begin{aligned} a_{\alpha\beta} &= a_\alpha + j a_\beta \\ &= \sqrt{\frac{2}{3}} \begin{bmatrix} 1 & \frac{-1+j\sqrt{3}}{2} & \frac{-1-j\sqrt{3}}{2} \end{bmatrix} \begin{bmatrix} a_u \\ a_v \\ a_w \end{bmatrix} \end{aligned} \tag{3.1}$$

The active and reactive power injected from the inverter to the grid is given by

$$\begin{aligned} p[i] &= v_{C\alpha}[i]i_{o\alpha}[i] + v_{C\beta}[i]i_{o\beta}[i] \\ q[i] &= v_{C\alpha}[i]i_{o\beta}[i] - v_{C\beta}[i]i_{o\alpha}[i] \end{aligned} \tag{3.2}$$

where $p[i]$ and $q[i]$ are the active and reactive power, respectively, which are the values at time $t=i\ T_s$ with T_s as the sampling period. The complex power can be written as

$$\begin{aligned} p[i] + jq[i] &= (v_{C\alpha}[i] + jv_{C\beta}[i])^{*}(i_{o\alpha}[i] + ji_{o\beta}[i]) \\ &= v^{*}_{C\alpha\beta}[i]i_{o\alpha\beta}[i] \end{aligned} \tag{3.3}$$

where * denotes the complex conjugate.

The state space model of the grid-forming inverter based on the complex vectors in the $\alpha\beta$-frame can be written as follows:

$$\begin{aligned} \dot{\boldsymbol{x}}_{\alpha\beta}(t) &= \boldsymbol{A}_c \boldsymbol{x}_{\alpha\beta}(t) + \boldsymbol{b}_c u_{\alpha\beta}(t) + \boldsymbol{h}_c i_{o\alpha\beta}(t) \\ y_{\alpha\beta}(t) &= \boldsymbol{c}_c \boldsymbol{x}_{\alpha\beta}(t) \end{aligned} \tag{3.4}$$

where

$$x^{T}_{\alpha\beta} = \begin{bmatrix} i_{L\alpha\beta} & v_{C\alpha\beta} \end{bmatrix},\quad \boldsymbol{A}_c = \begin{bmatrix} -R/L & -1/L \\ 1/C & 0 \end{bmatrix}, \boldsymbol{b}_c = \begin{bmatrix} E/2L \\ 0 \end{bmatrix}, \boldsymbol{h}_c = \begin{bmatrix} 0 \\ -1/C \end{bmatrix}, \boldsymbol{c}_c = \begin{bmatrix} 0 & 1 \end{bmatrix} \tag{3.5}$$

The vectors $\boldsymbol{x}_{\alpha\beta}$ and $u_{\alpha\beta}$ are the state variables and the system input respectively, and $i_{o\alpha\beta}$ is the injected current to the grid, considered as a perturbation in this case. The output $y_{\alpha\beta}$ is the voltage across the capacitor. It is noted that this system is an SISO system and a linear time-invariant (LTI) system.

3.1.2 Design of droop control

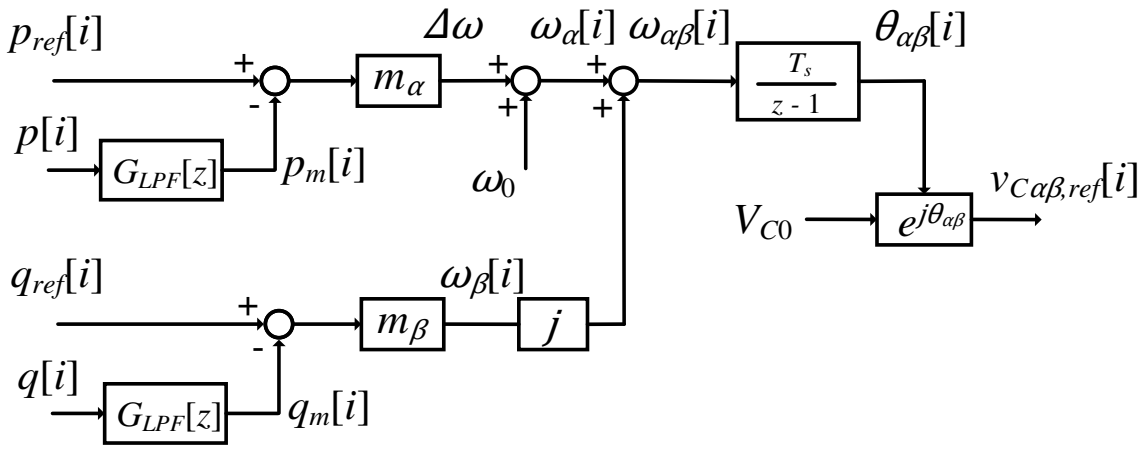

Fig. 3-2. Proposed complex droop control.

Fig. 3-2. shows the proposed complex droop control. A complex angular frequency $\omega_{\alpha\beta}[i]$ and a complex phase angle $\theta_{\alpha\beta}[i]$ are introduced in the proposed control [11]. The complex angular frequency is composed of the P-f and Q-V droop components that are placed in the real and imaginary parts respectively. It can be obtained as follows:

$$\omega_{\alpha\beta}[i] = \{m_\alpha(p_{ref}[i] - p_m[i]) + \omega_0\} + j\{m_\beta(q_{ref}[i] - q_m[i])\} \tag{3.6}$$

The complex phase angle $\theta_{\alpha\beta}[i]$ computes as discrete integral of the complex angular frequency $\omega_{\alpha\beta}[i]$.

$$\theta_{\alpha\beta}[i] = \frac{T_s}{z-1}\omega_{\alpha\beta}[i] \tag{3.7}$$

The amplitude and the phase rotation of the voltage reference $v_{C\alpha\beta,ref}[i]$ can be expressed with the complex exponential form:

$$v_{C\alpha\beta,ref}[i] = V_{C0}e^{j\theta_{\alpha\beta}[i]} = (V_{C0}e^{-\theta_\beta[i]})e^{j\theta_\alpha[i]} \tag{3.8}$$

where V_{C0} is the fundamental voltage amplitude. It can be seen from the equations above, (3.6), (3.7), and (3.8), that the complex phase angle can express both the magnitude and the phase angle of the voltage reference, that is, that $\theta_\alpha[i]$ is derived from the active power droop and contributes as the phase angle of the voltage reference as $e^{j\theta_\alpha[i]}$, while $\theta_\beta[i]$ is derived from the reactive power droop and $V_{C0}\,e^{-\theta_\beta[i]}$ characterizes the magnitude of the voltage reference. It is also noted that the integration of $\omega_{\alpha\beta}[i]$ works as an integral compensation for both active and reactive powers and eliminates steady-state errors.

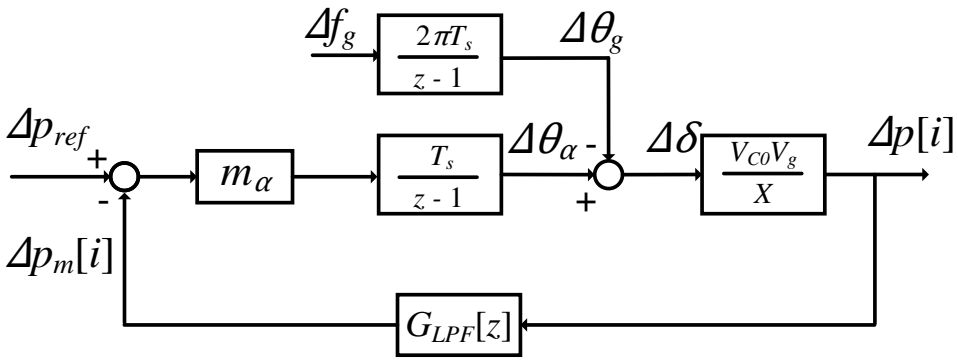

Fig. 3-3 Active power control loop around an operating point.

The droop gains, m_α and m_β, are tuned based on transfer functions around an operating point. Equation (1.3) indicates that active and reactive power is coupled, that is, they are both affected by fluctuations of phase difference as well as of voltage amplitude. Although this coupling complicates the tuning of droop gains, at operating points in equations (1.6)and (1.7), they are tuned independently since active and reactive power are decoupled.

First, the P-f droop gain m_α is tuned. The control system of the active power around an operating point derived from equations (1.6), (3.6), and (3.7) is shown in Fig. 3-3, where the phase difference of the voltages is $\Delta\delta = \Delta\theta_\alpha - \Delta\theta_g$. In this control, the voltage control loop is neglected since it should be fast enough to

not affect the power control. The transfer functions from the reference of the active power $\Delta p_{ref}[i]$ and the grid frequency $\Delta f_g[i]$ to the inverter output active power $\Delta p[i]$ are as follows:

$$\Delta p[i] = G_p[z]\Delta p_{ref}[i] + G_f[z]\Delta f_g[i] \tag{3.9}$$

where

$$G_p[z] = \frac{\frac{V_{C0}V_g}{X}\frac{m_\alpha T_s}{z-1}}{1-\frac{V_{C0}V_g}{X}\frac{m_\alpha T_s}{z-1}G_{LPF}[z]}$$
$$G_f[z] = -\frac{2\pi\frac{V_{C0}V_g}{X}\frac{T_s}{z-1}}{1-\frac{V_{C0}V_g}{X}\frac{m_\alpha T_s}{z-1}G_{LPF}[z]} \tag{3.10}$$

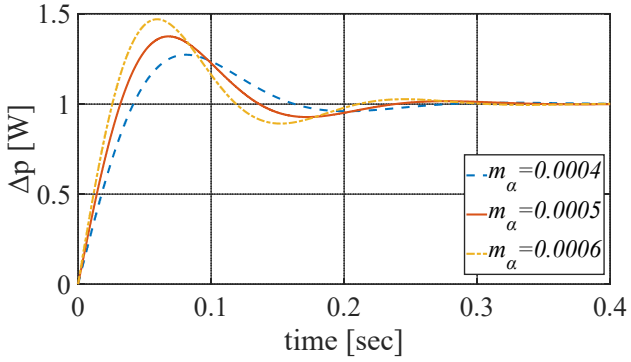

(a) Δp_{ref}

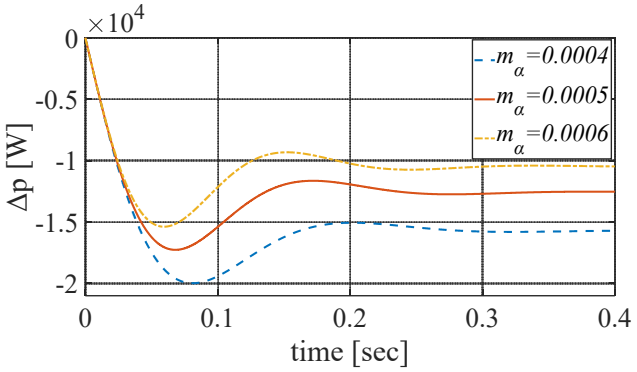

(b) Δf_g

Fig. 3-4. Step response for active power p

Table 3-1. System parameters.

Parameters	**Values**
DC voltage E	400 [V]
Line-voltage amplitude V_{C0}	200 [V]
Fundamental frequency f_0	50 [Hz]
Filter inductance L	0.76 [mH]
Filter resistance R	0.055 [Ω]
Filter Capacitance C	20 [μF]
Sample frequency f_s	10 [kHz]
Grid inductance L_g	1.73 [mH]
Grid resistance R_g	0.055 [Ω]
Reference of active power p_{ref}	1000 [W]
Reference of reactive power q_{ref}	0 [var]

Table 3-1 presents the system parameters. For attenuating the noise of measured power, the cut-off frequency of the low-pass filter is set to 31.4 rad/s (5Hz), which is 1/10 of the fundamental frequency. Fig. 3-4.(a)(b) show the step responses from the reference active power Δp_{ref} and grid frequency Δf_g to the measured active power, respectively, where the droop gain is set to some parameters. These indicate that increase of the droop gain results in a higher peak of overshoot for the step response from the reference of the active power, while it enables suppression of the active power droop when the grid frequency is fluctuated. The active power droop gain is set to m_α =0.0005 [rad/(s･W)], where the trade-off described above is taken into account. With this parameter, the peak of the overshoot of active power p is 1.37 times higher than the reference and the settling time is 0.24 sec, which is here defined as 2% error range from the reference. The peak of the overshoot of measured active power p_m is 1.20 times higher than the reference and the settling time is 0.22 sec.

Second, the Q-V droop gain m_β is also tuned. The control system of the reactive power around an operating point derived from equations (1.7), (3.7), (3.6), (3.7), and (3.8) is shown in Fig. 3-5. Increase in $\Delta\theta_\beta$ results in the reduction of amplitude ΔV_c due to the term $-V_{C0}e^{-\theta_{\beta 0}}$. A transfer function from the reference of the reactive power $\Delta q_{ref}[i]$ to the inverter output reactive power $\Delta q[i]$ is as follows:

$$\Delta q[i] = G_q[z]\Delta q_{ref}[z] \tag{3.11}$$

where

$$G_q[z] = \frac{\frac{V_{g0}-2V_{C0}}{X}(-V_{C0}e^{-\theta_\beta})\frac{m_\beta T_s}{z-1}}{1-\frac{V_{g0}-2V_{C0}}{X}(-V_{C0}e^{-\theta_\beta})\frac{m_\beta T_s}{z-1}G_{LPF}[z]} \tag{3.12}$$

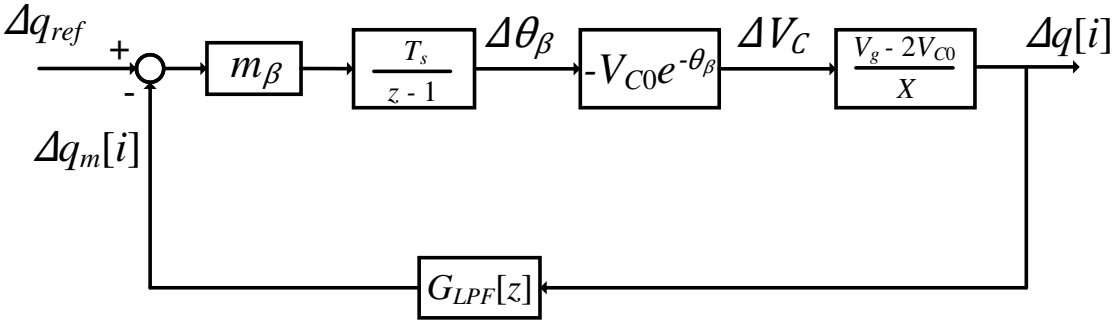

Fig. 3-5. Reactive power control loop around an operating point.

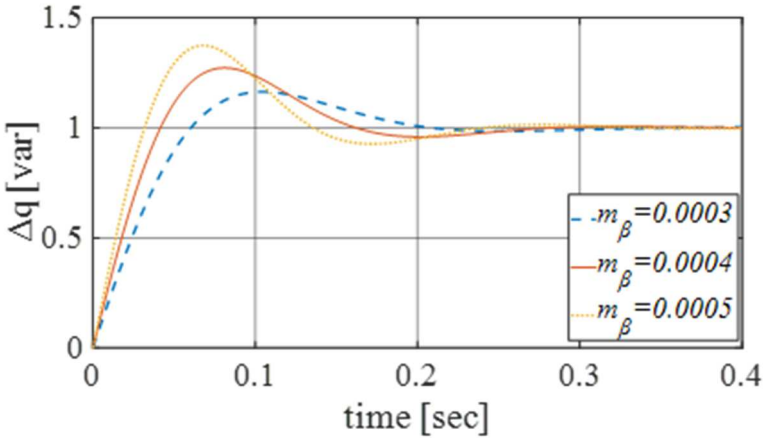

Fig. 3-6. Step response for reactive power q.

Fig. 3-6. shows a step response from the reference reactive power Δq_{ref} to the measured active power Δq, where the Q-V droop gain is set to some parameters. Thanks to the integrator, the reactive power can be tracked to the reference. It also indicates that the increase of the Q-V droop gain results in a higher peak of overshoot for the step response from the reference of the reactive power. The Q-V droop gain is set to m_β =0.0004 [rad/(s·var)], where the peak of the overshoot is 1.27 times higher than the reference and the settling time is 0.24 sec.

3.1.3 Design of voltage control

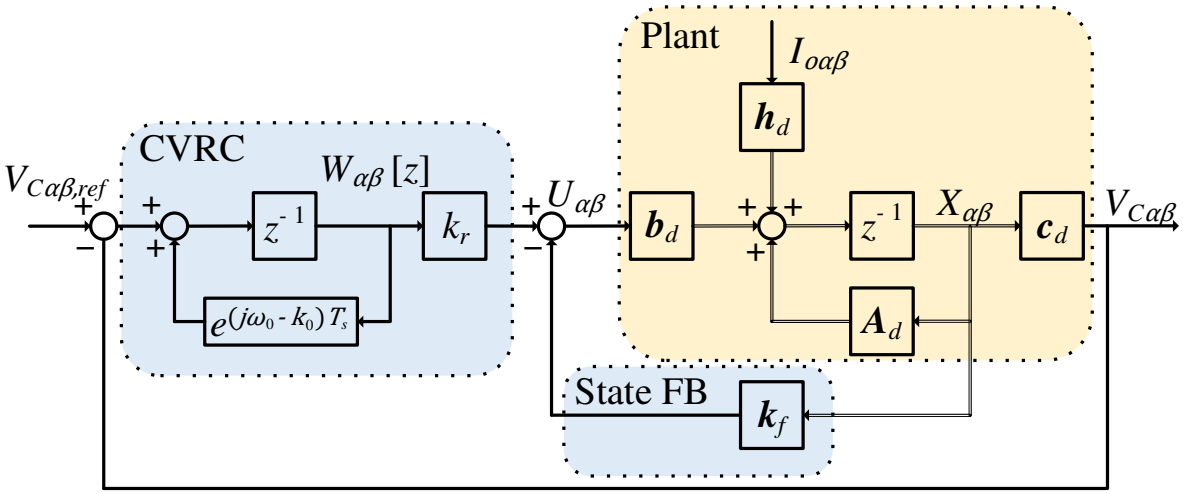

Fig. 3-7. Block diagram of voltage control system consisting of CVRA and state-feedback control.

For the voltage controller design in the discrete-time domain, equations (3.4) and (3.5) should be discretized as follows:

$$\begin{aligned} \boldsymbol{x}_{\alpha\beta}[i+1] &= \boldsymbol{A}_d \boldsymbol{x}_{\alpha\beta}[i] + \boldsymbol{b}_d u_{\alpha\beta}[i] + \boldsymbol{h}_d i_{o\alpha\beta}[i] \\ y_{\alpha\beta}[i] &= \boldsymbol{c}_d \boldsymbol{x}_{\alpha\beta}[i] \end{aligned} \tag{3.13}$$

where

$$\begin{aligned} \boldsymbol{A}_d &= e^{\boldsymbol{A}_c T_s}, \quad \boldsymbol{b}_d = \int_0^{T_s} e^{\boldsymbol{A}_c T_s} d\tau \boldsymbol{b}_c \\ \boldsymbol{c}_d &= \boldsymbol{c}_c, \quad \boldsymbol{h}_d = \int_0^{T_s} e^{\boldsymbol{A}_c T_s} d\tau \boldsymbol{h}_c \end{aligned} \tag{3.14}$$

The voltage reference represented in complex vectors can be written as $v_{C\alpha\beta,ref}(t)=V_{amp}\, e^{j\omega t}$ in the continuous-time domain, where ω and V_{amp} are derived from the complex droop control described in Section 3.1.2. Since the voltage reference $v_{C\alpha\beta,ref}(t)$ provided from the droop control is discretized, the z-transform should be considered.

$$Z\left\{v_{C\alpha\beta,ref}(t)\right\} = \frac{zV_{C0}}{z - e^{j\omega_0 T_s}} \tag{3.15}$$

Based on the internal model principle, the discrete voltage regulator should have the denominator of equation (3.15) for tracking the reference, called the CVRC [41] [42]. A proposed voltage regulation system is shown in Fig. 3-7, where the voltage regulation is composed of a state-feedback control and the CVRC, whose $\boldsymbol{k}_f$, and k_r are a state-feedback gain vector and CVRC gain, respectively, ω_0 is the fundamental frequency in the grid, and k_0 is a damping of the CVRC. The controlled system of augmented matrices can be written as follows:

$$
\begin{aligned}
\hat{\boldsymbol{x}}_{\alpha\beta}[i+1] &= \hat{\boldsymbol{A}}_d\,\hat{\boldsymbol{x}}_{\alpha\beta}[i] + \hat{\boldsymbol{b}}_d\,u_{\alpha\beta}[i] + \hat{\boldsymbol{h}}_d\,i_{o\alpha\beta}[i] \\
&\quad + \hat{\boldsymbol{g}}_d\,v_{C\alpha\beta,ref}[i] \\
y_{\alpha\beta}[i] &= \begin{bmatrix}\boldsymbol{c}_d & 0\end{bmatrix}\hat{\boldsymbol{x}}_{\alpha\beta}[i] \\
u_{\alpha\beta}[i] &= -\hat{\boldsymbol{k}}\,\hat{\boldsymbol{x}}_{\alpha\beta}[i]
\end{aligned}
\tag{3.16}
$$

where

$$
\begin{aligned}
&\hat{\boldsymbol{x}}_{\alpha\beta} = \begin{bmatrix}\boldsymbol{x}_{\alpha\beta} \\ w_{\alpha\beta}\end{bmatrix}, \hat{\boldsymbol{k}} = \begin{bmatrix}\boldsymbol{k}_f & -k_r\end{bmatrix} \\
&\hat{\boldsymbol{A}}_d = \begin{bmatrix}\boldsymbol{A}_d & \boldsymbol{0} \\ \boldsymbol{c}_d & e^{(j\omega_0 - k_0)T_s}\end{bmatrix}, \hat{\boldsymbol{b}}_d = \begin{bmatrix}\boldsymbol{b}_d \\ 0\end{bmatrix}, \hat{\boldsymbol{h}}_d = \begin{bmatrix}\boldsymbol{h}_d \\ 0\end{bmatrix}, \hat{\boldsymbol{g}}_d = \begin{bmatrix}\boldsymbol{0} \\ 1\end{bmatrix}
\end{aligned}
\tag{3.17}
$$

$w_{\alpha\beta}$ is a state variable for CVRC. It is noted from equation (3.16) that the number of state variables including the controller is 3, but if the system is modelled using the real vectors it is 6. Moreover, the model based on the complex vectors is the SISO system, while a system modelled in the real vectors is the MIMO system. From these points of view, the modeling and design of the controller using complex vectors are simpler compared to real vector modeling.

The quadratic optimal regulator problem is applied to determine the control gain vector $\hat{\boldsymbol{k}}$ so as to minimize the performance index,

$$
J = \frac{1}{2}\sum_{i=0}^{\infty}\left\{(\hat{\boldsymbol{x}}^*_{\alpha\beta}[i])^T\boldsymbol{Q}\hat{\boldsymbol{x}}_{\alpha\beta}[i] + u^*_{\alpha\beta}[i]ru_{\alpha\beta}[i]\right\} \tag{3.18}
$$

where $\boldsymbol{Q}$ is a positive-definite (or positive-semidefinite) Hermitian or real symmetric matrix and r is a positive-scalar. Note that the first term on the right side of the equation is related to the convergence speed of each of the state variables, and the second term is the expenditure of the energy of the control signals. The matrix $\boldsymbol{Q}$ and the scalar r determine the relative importance of the convergence speed and the expenditure of this energy, respectively. An advantage of the LQR method over the pole-placement method is that it provides a systematic way of computing the state-feedback control gain vector.

In this thesis, the response time of the voltage control system is designed to be 10 times slower than the droop control. Since the absolute value of poles for the droop control is $|\lambda_p|$= 0.9984, which is derived from the transfer function $G_p[z]$ in equation (3.9), that of the voltage control should be exp(10log$|\lambda_p|$)= 0.9841, which is 10 times slower than the droop control [43]. The weights $\boldsymbol{Q}$ and r in equation (3.18) are tuned so that an average of the absolute value of eigenvalues defined as λ_{vi} (i=1~3) for the closed-loop voltage control ($\hat{\boldsymbol{A}}_d - \hat{\boldsymbol{b}}_d\hat{\boldsymbol{k}}$) is set to 0.9841. First, the weight $\boldsymbol{Q}$ for all state variables is set to be a third-order unit matrix, and then the weight r in which the control input becomes smaller by increasing, indicating that the response has become equivalently slower, is tuned to obtain complex gain vector $\hat{\boldsymbol{k}}$. The poles of the closed-loop voltage control system are tuned based on the flow chart presented in Fig. 3-8. The root loci of the three eigenvalues λ_{vi}, or poles, of the voltage control system during this tuning are shown in Fig. 3-9. As the weight r is increased, the response becomes slower and the poles of the voltage control system become larger toward

the outside. The average eigenvalue is set to 0.9841 at r =9.286×10^7. The complex gains $\boldsymbol{k}_f$ and k_r, LQR weights, and poles of the voltage control system are shown in Table 3-2.

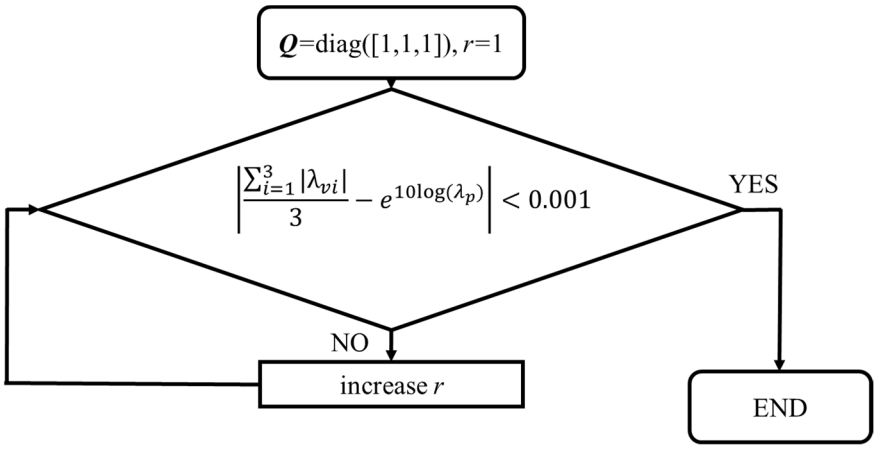

Fig. 3-8. Flow chart of voltage control tuning.

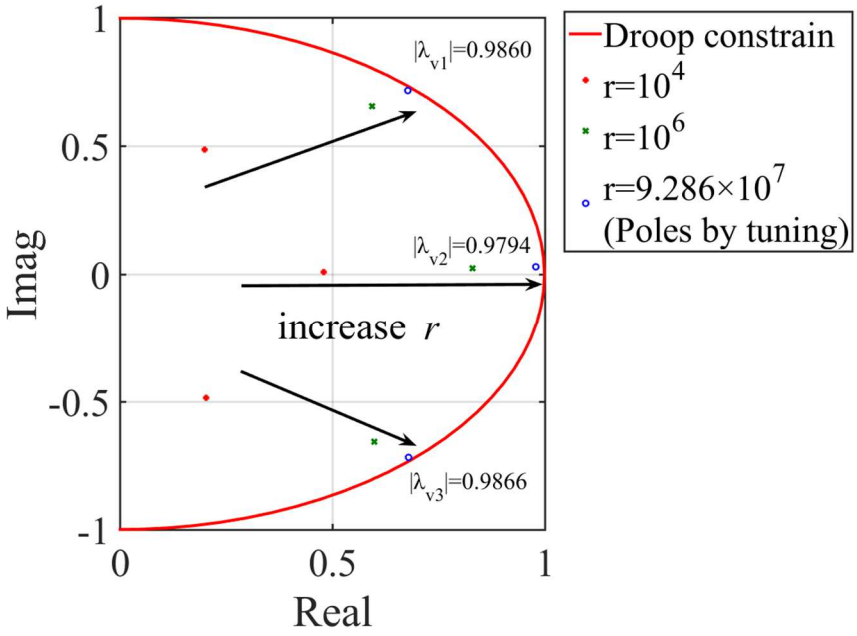

Fig. 3-9. Root locus for voltage control system.

Table 3-2. Controller gains, LQR weights, and eigenvalues.

Active power droop gain m_α	0.0005 [(rad/(s·W)]
Reactive power droop gain m_β	0.0004 [rad/(s·var)]
Cut-off frequency ω_c	31.4 [rad/s]
CVRC damping coefficient k_0	0
Feedback gain $\boldsymbol{k_f}$	[1.417×10^{-3}+j1.942 ×10^{-5} 6.213×10^{-6}+j9.253 ×10^{-6}]
CVRC gain k_r	9.671×10^{-5}+j4.943 ×10^{-6}
LQR weight $\boldsymbol{Q}$	diag[1 1 1]
LQR weight r	9.286×10^{7}
Eigenvalue λ_{v1}	0.6774 + j0.7164
Eigenvalue λ_{v2}	0.9789 + j0.0307
Eigenvalue λ_{v3}	0.6778 - j0.7168

To analyze the closed-loop voltage control system, transfer functions from the voltage reference $V_{C\alpha\beta,ref}[z]$ and the output current $I_{o\alpha\beta}[z]$ to the output voltage $V_{C\alpha\beta}[z]$ are derived as follows:

$$V_{C\alpha\beta}[z] = G_v[z]V_{C\alpha\beta,ref}[z] - Z_o[z]I_{o\alpha\beta}[z] \tag{3.19}$$

where, $G_v[z]$ is the closed-loop transfer function from $V_{C\alpha\beta,ref}[z]$ to $V_{C\alpha\beta}[z]$, and $Z_o[z]$ is the closed-loop output impedance, where the power control is not taken into account, as given by,

$$\begin{cases} G_v[z] = \boldsymbol{c}_d\left\{z\boldsymbol{I} - \boldsymbol{A}_d + \boldsymbol{b}_d\left(\dfrac{k_r\boldsymbol{c}_d}{z - e^{(j\omega_0 - k_0)T_s}} + \boldsymbol{k}_f\right)\right\}^{-1} \cdot \boldsymbol{b}_\mathbf{d} \cdot \dfrac{k_r}{z - e^{(j\omega_0 - k_0)T_s}} \\ Z_o[z] = -\boldsymbol{c}_d\left\{z\boldsymbol{I} - \boldsymbol{A}_d + \boldsymbol{b}_d\left(\dfrac{k_r\boldsymbol{c}_d}{z - e^{(j\omega_0 - k_0)T_s}} + \boldsymbol{k}_f\right)\right\}^{-1} \cdot \boldsymbol{h}_\mathbf{d} \end{cases} \tag{3.20}$$

Gain and phase of $G_v[z]$ around the fundamental frequency should be 0 dB and 0 degrees, respectively, for the tracking performance; that is, in the steady state, the output voltage can be followed to the reference voltage without amplitude error, phase-lag, and phase-lead. The output impedance $Z_o[z]$ should be as small as possible in order to enhance the load disturbance rejection capability. This is indicated by equation (3.19), which shows that the output current minimally affects the output voltage.

To compare the performance of different control gains, the frequency and time responses are analyzed for three scenarios, where the closed-loop voltage control systems are designed to be 5, 10, and 20 times slower than the power control, where the control gains are determined by the flow-chart presented in Fig. 3-8. The frequency characteristics for each LQR weight are shown in Fig. 3-10. It indicates that the gains and phases of $G_v[z]$ at the fundamental frequency are all 0 dB and 0 degrees, respectively, while the output impedance $Z_o[z]$ is reduced by smaller weight r, especially at lower frequency. Fig. 3-11. shows time responses from the reference voltage to the output voltage. The increase of weight r results in faster response,

but also causes overshoot in the transient state. It is also noted in the next section in detail that a slower voltage response affects the coupling between active and reactive powers.

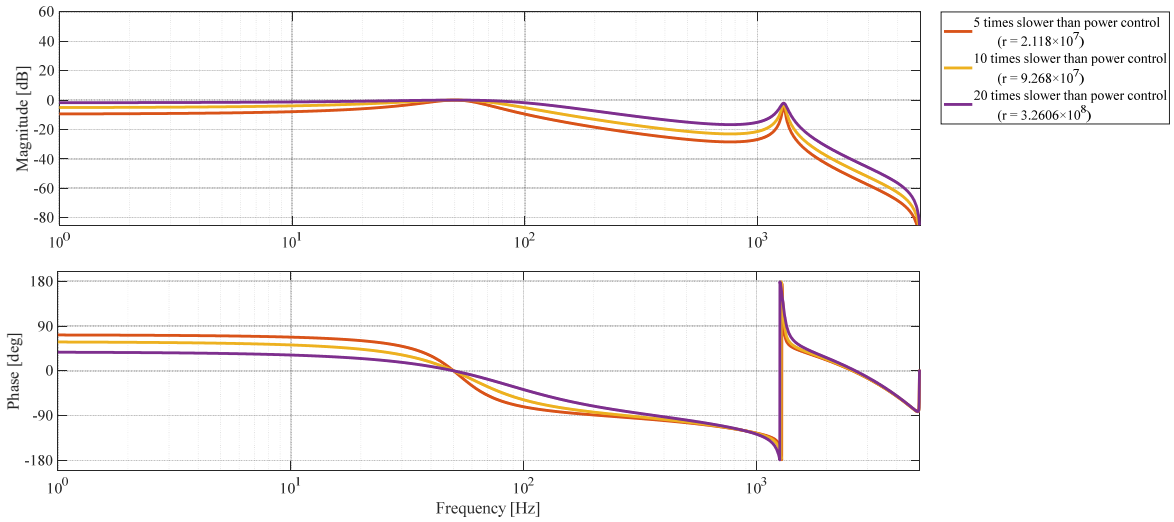

(a) $G_v[z]$

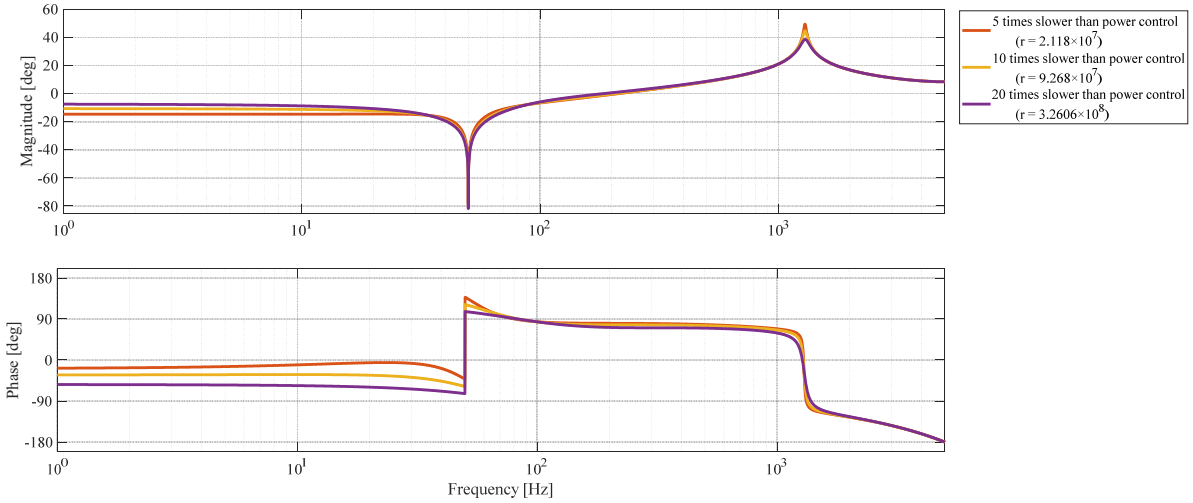

(b) $Z_o[z]$

Fig. 3-10. Comparison of frequency responses for different LQR weights.

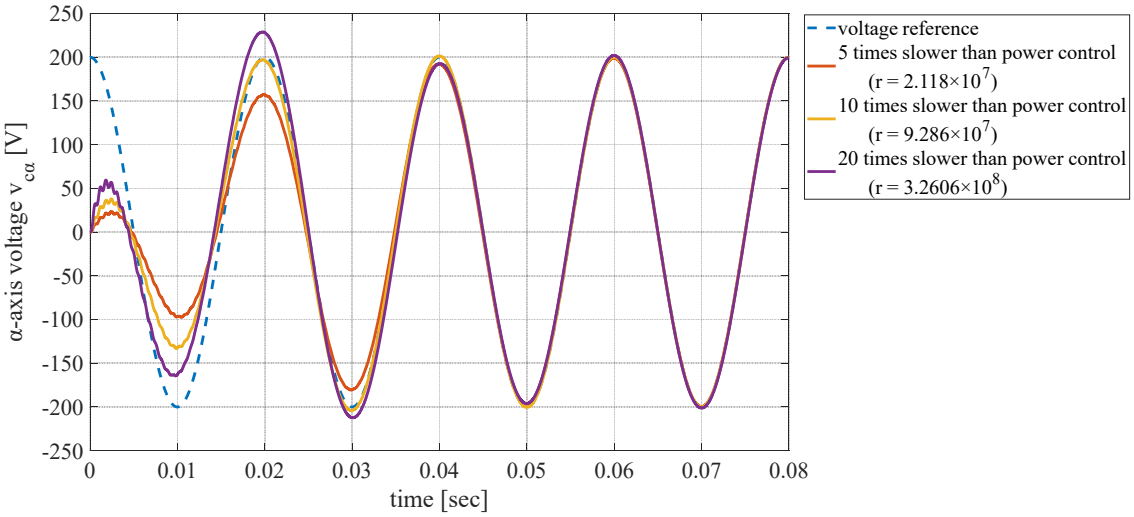

(a) Time response for α-axis voltage.

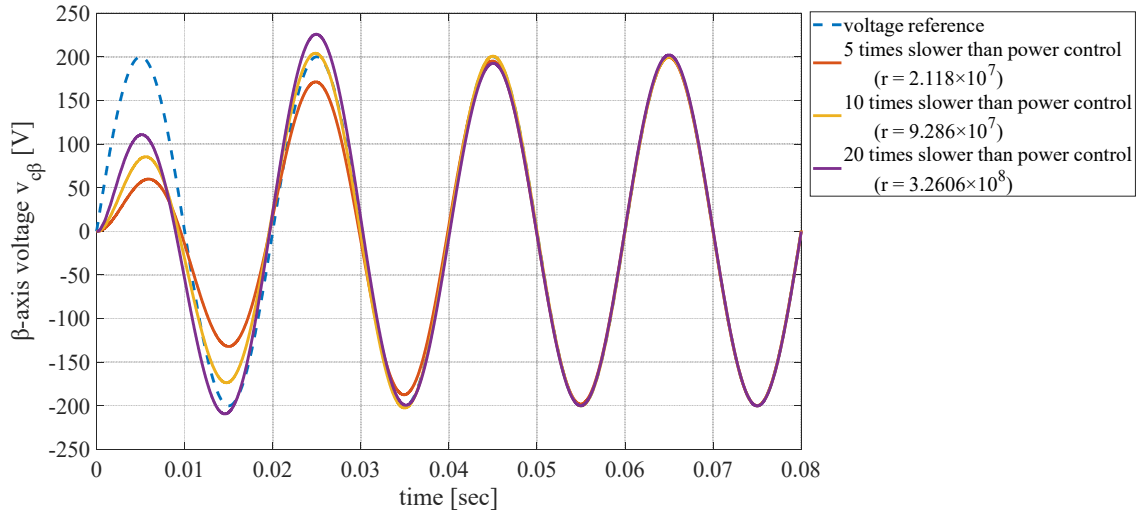

(b) Time response for β-axis voltage.

Fig. 3-11. Comparison of time responses of output voltage for different LQR weights.

3.2 Simulation and experimental results

Performances with different controller gains are compared by simulations. Since controller gains for active and reactive power and voltage response were tuned individually and there are some couplings among them, the comparison of performances with all controls combined is needed. Simulations are executed by Saber RD [44] and its C control program is the same as that in the experiments described below. The simulation system consists of the circuit shown in Fig. 3-1, where a switching model is applied, and the parameters are based on Table 3-1 and Table 3-2.

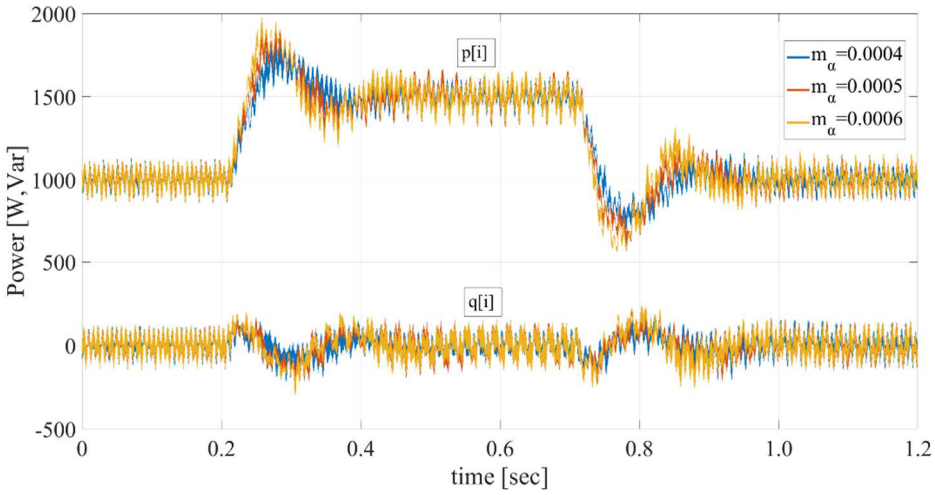

Fig. 3-12. Active power setpoint change and its coupling on the reactive power by simulations.

Fig. 3-12 shows the active power setpoint change and its coupling on the reactive power. Time responses of the active power almost coincide with those shown in Fig. 3-4, and increase of the droop gain m_α results in a higher peak of overshoot. The coupling with the reactive power, which is not represented in equation (3.9), can also be confirmed, and increasing the active power gain m_α makes the coupling slightly larger.

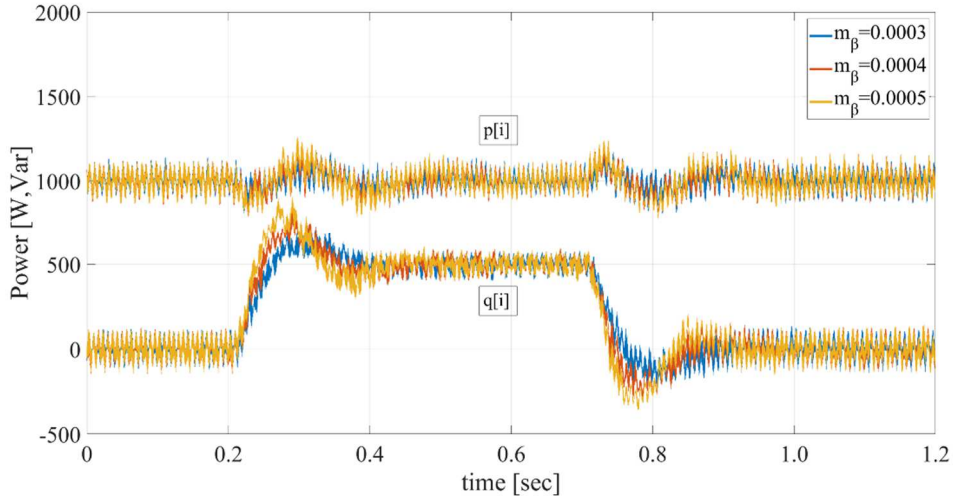

Fig. 3-13. Reactive power setpoint change and its coupling on the active power by simulations.

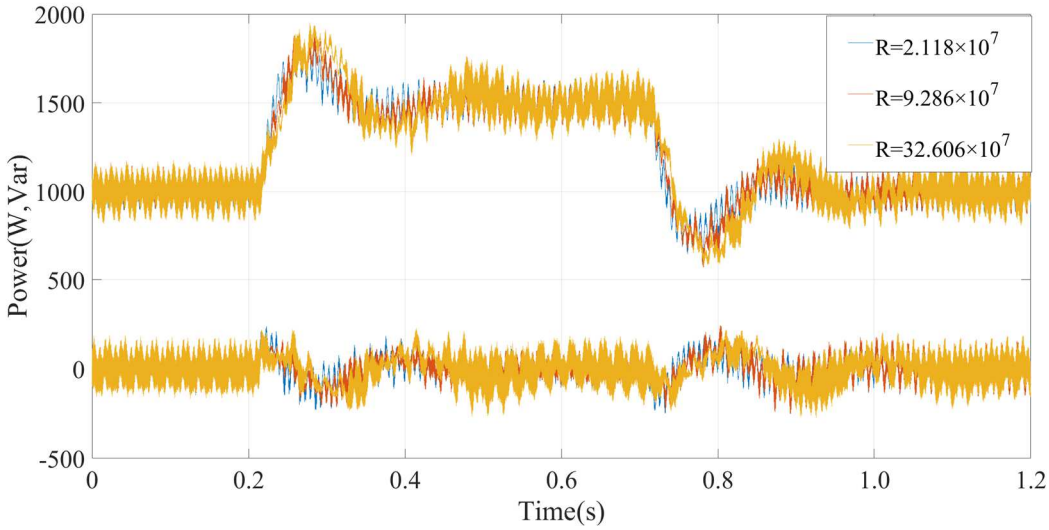

Fig. 3-14. Effects of different voltage responses on coupling of active and reactive power.

Fig. 3-13 shows the reactive power setpoint change and its coupling on the active power. The same tendency can be observed in the response of the reactive power as that of the active power. Increase of the droop gain m_β results in a higher peak of overshoot and makes the coupling slightly larger.

Fig. 3-14 shows the effects of different voltage responses on the coupling of active and reactive power. It indicates that the slower the voltage response is, the slower the active power is converged, which results in the reactive power also being converged slower.

The proposed complex control is also validated by experiments. An experimental system consists of the circuit shown in Fig. 3-1 and parameters based on Table 3-1 and Table 3-2. A photograph of the experimental set-up is shown in Fig. 3-15. A three-phase SiC inverter driven by a DSP (TMS320C6657) based digital control system is connected to a grid impedance and a grid simulator via an LC filter.

Fig. 3-16 shows u-phase capacitor voltage v_{cu} and output current i_{ou} in the steady state, where the active and reactive power are controlled to 1000 W and 0 var, respectively. It is evident that the phase of the output current is controlled the same as that of the capacitor voltage for setting the reactive power to 0 var, which meant that the power factor is 1. Although there is some distortion in the current waveform, the RMS voltage and current are controlled to 115 V and 2.9 A, respectively, to output 1000 W to the grid.

The proposed control in the transient state is also investigated by an experiment shown in Fig. 3-17. The reference of the active power is controlled to 1000 W, changed in step to 1500 W at 0.5 sec, and changed back to 1000 W at 1.5 sec, where the reactive power is constantly controlled to 0 var. The active and reactive power is controlled to the reference values in the steady state. This is because the complex droop control has a desirable feature in that the integration for the complex phase computation described in equation (3.7) works for the active and reactive powers and eliminates steady-state errors. The peak of the overshoot of measured active power is 1.30 times higher than the reference and the settling time is 0.27 sec, which is slightly different from the design values of 1.20 times and 0.24 sec on page 42. The main reasons for these deviations are that the coupling between active and reactive power was neglected in the derivation of equations (3.9) and (3.11) by the approximation at the operating point, and the response of the voltage control is also neglected when designing the droop control gains, but the approximation is suitable for tuning the controller gains.

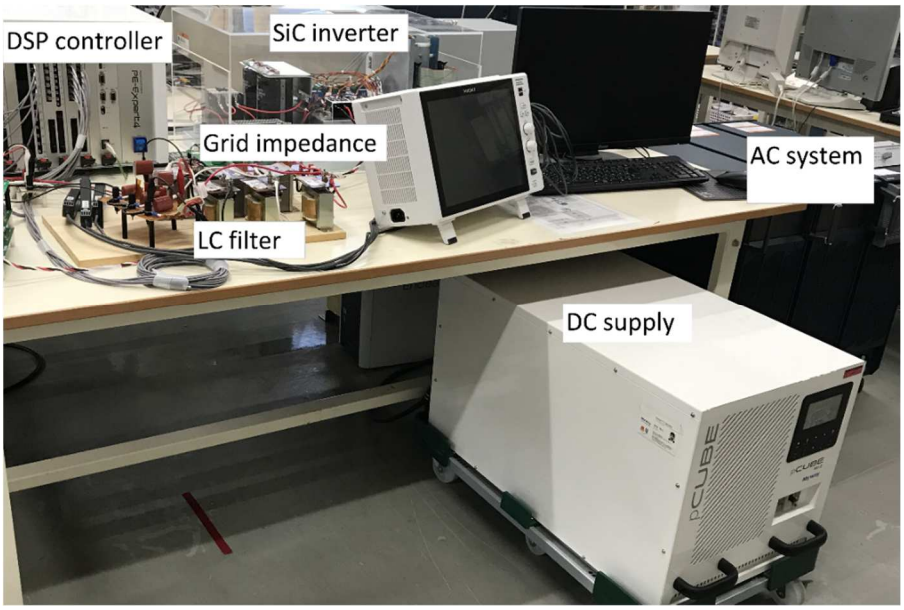

Fig. 3-15. Experimental system set-up.

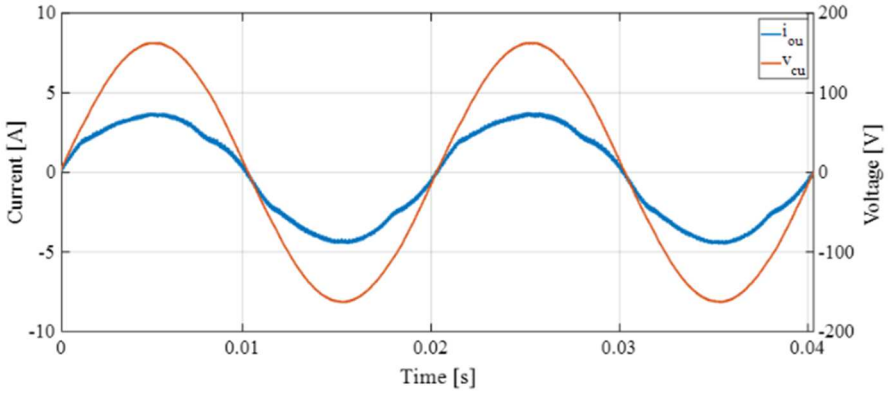

Fig. 3-16. Voltage and current waveforms in steady state by experiment.

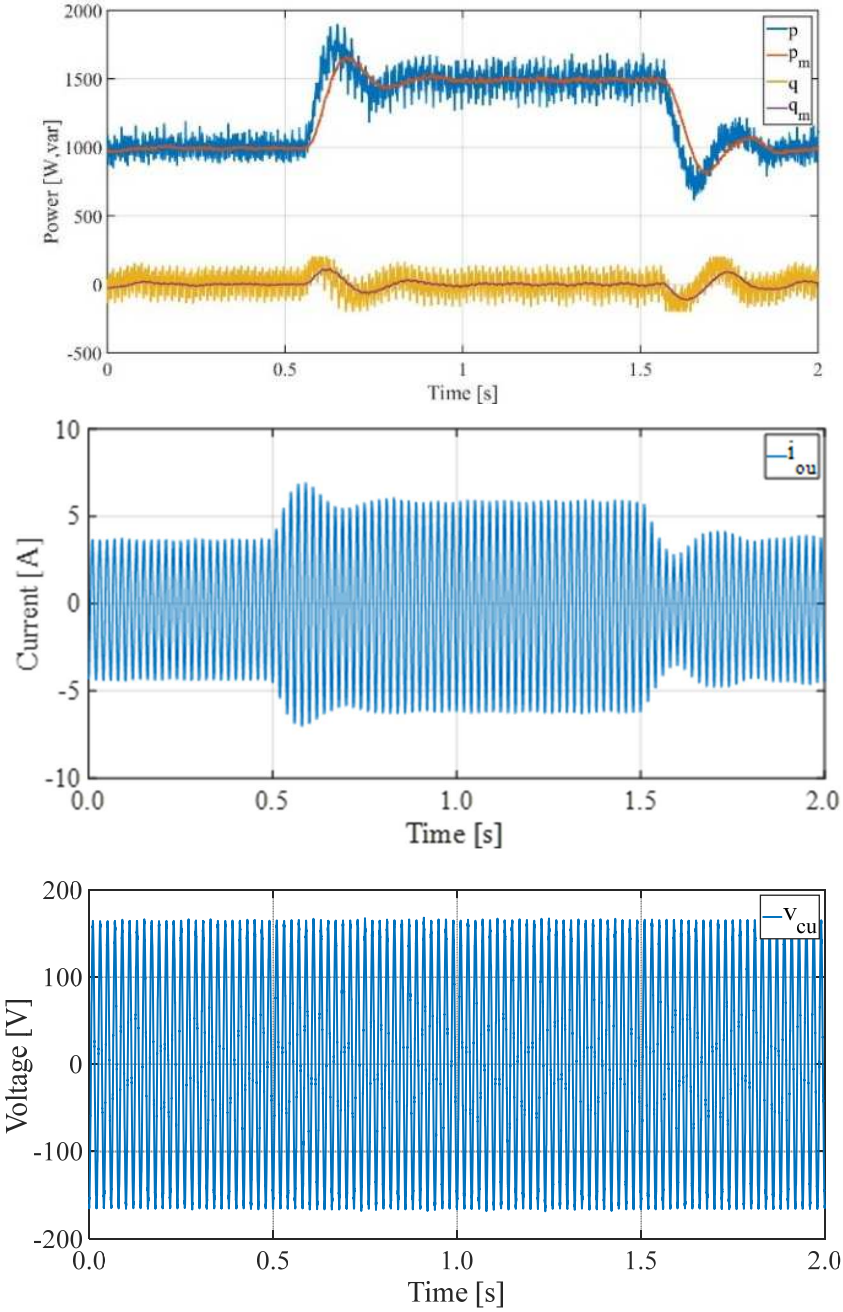

Fig. 3-17. Transient power response by experiment.

3.3 Summary

This section proposes a control system design method in a $\alpha\beta$-frame for a grid-forming inverter using complex vectors, which can be summarized in the following five points.

(1) The proposed droop control is a novel method in the $\alpha\beta$-frame that does not require the estimation of the reference phase needed in the dq conversion.

(2) The proposed controller utilizes the complex vector theory to treat state variables as complex vectors, and the MIMO system with three-phase $\alpha\beta$ components can be described concisely as a complex SISO system, which simplifies the design and analysis of control systems.

(3) It is verified by simulations and experiments that the proposed complex droop controller can control active and reactive power without steady-state deviation.

(4) The gains of complex droop control are designed by deriving the transfer function at the operation point to balance the trade-off between the overshoot suppression of the step response and the inverter output power in the frequency fluctuation of the grid.

(5) The gains for the voltage control system are determined by tuning the weight of the input r so that its response time is 10 times slower than the droop controller based on the LQR.

4. Conclusions

This dissertation examined controller schemes, tuning methods, and the analysis of the stability for grid-forming inverters. Two controller schemes were proposed: the first controller is composed of a basic droop controller for power control and a state-feedback controller and integral compensator for voltage regulation in the *dq*-domain, and the second controller is based on complex vector theory in the $\alpha\beta$-domain and is composed of a complex droop controller and a state-feedback controller with CVRC.

In Section 1, the background and outline of this research were described and the characteristics of grid-following and grid-forming controls were discussed. The electrical system must guarantee the fixed frequency and voltage amplitude. Grid-forming inverters can help the system frequency and voltage amplitude with emulated inertia, power sharing (which is implemented by the primary control such as the droop control and the VSM) and voltage regulation (which is implemented by the inner voltage controller). The system stability was also discussed in this section. Interactions between grid-connected inverters and the grid may destabilize the grid system because of the closed loop of the impedances. This stability can be analyzed by means of state-space analysis and impedance-based analysis.

In Section 2, a new voltage regulator was proposed. The proposed servo-system with a state-feedback and an integral compensator has 16 gains compared to the 8 gains of a cascaded PI controller; as such, the former has a greater degree of freedom. Controller gains are tuned based on the LQR and the participation factor. The participation factor helps in the determination of LQR weights since it indicates the sensitivity of an eigenvalue to a state variable. The performance of both the cascaded PI controller and the LQR were also compared by simulations. The proposed system generates a faster voltage response with lower overshoot and a small transient coupling effect between the active and reactive powers. The small-signal stability in the *dq*-frame was also analyzed by state-space analysis and the impedance-based method. These two analysis and simulation results were consistent. It was also validated that the proposed servo system has more stability margins than the cascaded PI controller.

In Section 3, the complex droop control and voltage controller based on complex vectors in the $\alpha\beta$-frame is proposed. The complex droop control is a novel method that does not require the estimation of the reference phase that is needed in the *dq* conversion. With complex vectors, the MIMO system with $\alpha\beta$ components can be described concisely as a complex SISO system, which simplifies the design and analysis of control systems. The gains of complex droop control are tuned by means of the small-signal transfer functions at the operating point to balance the trade-off between the overshoot suppression of the step response of the references and the droop characteristics. The gains for the voltage regulation are tuned based on the LQR so that its response time is 10 times slower than the droop control. This controller was investigated and validated by simulations and experiments.

The two proposed controls have simple control structures with a sufficient number of gains to place the system poles arbitrarily, and the proposed tuning methods can implement the required power and voltage

responses without trial and error. Therefore, the proposed controls can be considered two effective methods for grid-forming control.

5. References

[1] “エネルギー白書 2022”, 経済産業省, (2022)

[2] “日本のエネルギー”, 経済産業省, (2021)

[3] H. Bevrani,B. Francois,and T. Ise : MICROGRID DYNAMICS and CONTROL ,John Wiley & Sons, Inc, (2017)

[4] G. Denis, T. Prevost, M. Debry, F. Xavier, X. Guillaud, and A. Menze: “The Migrate project: the challenges of operating a transmission grid with only inverter-based generation. A grid-forming control improvement with transient current-limiting control”, IET Renewable Power Generation, Vol.12, No.5, pp. 523-529, (2018)

[5] “High Penetration of Power Electronic Interfaced Power Sources (HPoPEIPS)”, ENTSO-E, Technical, Mar. 2017.

[6] X. Wang and F. Blaabjerg: “Harmonic stability in power electronic-based power systems: concept, modeling, and analysis”, IEEE Transactions on Smart Grid, Vol 10, No. 3, May (2019)

[7] T. Kato, K. Inoue, and Y. Nakajima: “Stabilization of grid-connected inverter system with feed-forward control,” IEEE Energy Conversion Congress and Exposition (ECCE), pp. 3375-3382 (2017)

[8] C. Li: “Unstable operation of photovoltaic inverter from field experiences”, IEEE Trans. Power Del., Vol. 33, No. 2, pp. 1013–1015, Apr. (2018).

[9] I. Vieto and J. Sun: “Small-signal impedance modeling of type-III wind turbine”, in Proc. IEEE Power Energy Soc. General Meeting, Denver, CO, USA, pp. 1–5 (2015)

[10] Y. Xu, H. Nian, L. Chen, and T. Zheng: “Frequency coupling characteristic modeling and stability analysis of doubly fed induction generator”, IEEE Transactions on Energy Conversion, Vol. 33, No. 3, Sept. (2018)

[11] D.Yang, X. Wang, F. Liu, K. Xin, Y. Liu, and F. Blaabjerg: “Symmetrical PLL for SISO impedance modeling and enhanced stability in weak grid”, IEEE Transactions on Power Electronics, Vol. 35, No.2, Feb. (2020)

[12] T. Kato, K. Inoue, and Y. Donomoto: “Fast current-tracking control for grid-connected inverter with an LCL filter by sinusoidal compensation”, IEEE Energy Conversion Congress and Exposition (ECCE), (2011)

[13] T. Qoria: “Grid-forming control to achieve 100% power electronics interfaced power transmission systems”, Ecole doctorale sciences et metiers de l'ingenieur L2EP (2020)

[14] Q-C. Zhong and G.Weiss: “Synchronverters: inverters that mimic synchronous generators”, IEEE Transactions on Industrial Electronics, Vol. 58, No. 4, Apr. (2011)

[15] K. Sakimoto, Y. Miura, and T. Ise: “Characteristics of parallel operation of inverter type distributed generators operated by a virtual synchronous generator”, IEEJ Transactions on Power and Energy, Vol. 133, No. 2, pp. 186-194 (2012)

[16] J. Alipoor, Y. Miura, andT. Ise: “Power system stabilization using virtual synchronous generator with alternating moment of inertia”, IEEE Journal of Emerging and Selected Topics in Power Electronics, Vol. 3, No. 2, June (2015)

[17] K. Sakimoto, Y. Miura,and T. Ise: “Stabilization of a power system including inverter type distributed generators by the virtual synchronous generator”, IEEJ Transactions on Power and Energy, Vol. 132, No. 4, pp. 341-349 (2011)

[18] O. Mo, S. D’Acro, and J-A. Suul: “Evaluation of virtual synchronous machines with dynamic or quasi-stationary machine models”, IEEE Transactions on Industrial Electronics, Vol. 64, Issue 7, pp. 5952- 5962 (2017)

[19] M. Yu, R. Ierna, and H. Urdal: “Use of and inertia-less virtual synchronous machine within future power networks with high penetrations of converters”, IEEE Power Systems Computation Conference (PSCC), pp. 1-7 (2016)

[20] B. B. Johnson, S. V. Dhople, A. O. Hamadeh, and P. T. Krein: “Synchronization of parallel single-phase inverters with virtual oscillator control”, IEEE Transactions on Power Electronics, Vol. 29, No. 11, pp. 6124–6138 (2014)

[21] G.Denis, T. Prevost, P. Panciatici, X. Kestelyn, F. Colas, and X. Guillaud: “Review on potential strategies for transmission grid operations based on power electronics interfaced voltage sources”, IEEE Power & Energy Society General Meeting, pp. 1-5 (2015)

[22] J. Liu, Y. Miura, and T. Ise: “Comparison of dynamic characteristics between virtual synchronous generator and droop control in inverter based distributed generators”, IEEE Transactions on Power Electronics, Vol. 31, No. 5 (2016)

[23] V. Thomas, S. Kumaravel, and S. Ashok: “Virtual synchronous generator and its comparison to droop control in microgrids”, IEEE International Conference on Power, Instrumentation, Control and Computing (PICC), pp.1-4 (2018)

[24] R. Ofir, U. Markovic, P. Aristidou, and G. Hug: “Droop vs. virtual inertia: comparison from the perspective of converter operation mode”, IEEE International Energy Conference (ENERGYCON), pp. 1-6 (2018)

[25] S. D’Acro and J-A Suul: “Virtual synchronous machines classification of implementations and analysis of equivalence to droop controllers for microgrids”, IEEE Grenoble Conference, pp.1-7 (2013)

[26] S. D’Acro, J-A Suul, and O-B Fosso: “Automatic tuning of cascaded controllers for power converters using eigenvalue parametric sensitivities”, IEEE Transactions on Industry Applications, Vol. 51, No. 2, pp. 1743-1753 (2015)

[27] G. Denis, T. Prevost, P. Panciatici, X. Kestelyn, F.Colas, and X. Guillaud : “Improving robustness against grid stiffness with internal control of an AC voltage-controlled VSC”, IEEE Power and Energy Society General Meeting (PESGM), pp. 1-5 (2016)

[28] T. Qoria, F. Gruson, F. Colas. X. Guillaud,M-S. Debry,and T. Prevost: “Tuning of cascaded controllers for robust grid-forming Voltage Source Converter”, IEEE Power Systems ComputationConference (PSCC) (2018)

[29] Z. Li, C. Zang, P. Zeng, H. Yu, S. Li, and J. Bian: “Control of a grid-forming inverter based on sliding-mode and mixed H_2/H_∞ control”, IEEE Transactions on Industrial Electronics, Vol. 64, No. 5, May. (2017)

[30] D. Pullaguram, S. Mishra, N. Senroy, and M. Mukherjee: “Design and tuning of robust fractional order controller for autonomous microgrid VSC system”, IEEE Transactions on Industry Applications, Vol 54, No. 1, Jan /Feb (2018)

[31] L. Yicheng: “Impedance modeling and stability analysis of grid-interactive converters”, Aalborg University (2020)

[32] J. Sun: “Impedance-Based Stability Criterion for Grid-Connected Inverters”, IEEE Transactions on Power Electronics, Vol. 26, No 11, pp. 3075-3078 (2011)

[33] Z. Shen, “Online measurement of three-phase AC power system impedance in synchronous coordinates”, Ph.D. dissertation, Dept. of Elect. Eng., Virginia Tech, Blacksburg, USA (2012)

[34] T. Kato, K. Inoue, and M. Ueda: “Lyapunov-based digital control of a grid-connected Inverter with an LCL filter”, IEEE Journal of Emerging and Selected Topics in Power Electronics, Vol. 2, Issue 4, pp. 942-948 (2012)

[35] T. Kato, K. Inoue, and Y. Nakajima: “Stabilization of grid-connected inverter system with feed-forward control”, IEEE Energy Conversion Congress and Exposition (ECCE), pp. 3375-3382 (2017)

[36] I. Muller, Y. B. Blauth, C. E. Pereira, G. Gabiatti, and G. Bonan: “Simplifying the design of parallel-connected UPS inverters by means of the per unit system”, IEEE Brazilian Power Electronics Conference, pp.554-550 (2009)

[37] K. Ogata: “MATLAB for control engineers”, Upper Saddle River, New Jersey 07458

[38] N. Pogaku, M. Prodanovic, and T-C. Green: “Modeling, analysis and testing of autonomous operation of an inverter-based microgrid”, IEEE Transactions on Power Electronics, Vol. 22, No. 2, pp. 613- 625 (2007)

[39] S. Danielsen, O-B. Fosso, and T. Toftevaag: “Use of participation factors and parameter sensitivities in study and improvement of low frequency stability between electrical rail vehicle and power supply”, IEEE European Conference on Power Electronics and Applications, pp. 1-10 (2009)

[40] A. Emami-Naeini and R. L. Kosut: “The generalized Nyquist criterion and robustness margins with applications”, IEEE 51th Conference on Decision and Control, (2012)

[41] X. Quan, X. Dou, Z. Wu, M. Hu, H. Song, and A.Q Huang: “A novel dominant dynamic elimination control for voltage-controlled inverter”, IEEE Transactions on Power Electronics, Vol. 65, No.8, Aug. (2018)

[42] H. Yu, M.A. Awal, H. Tu, Y. Du, S. Lukic, and I. Husain: “Passivity-oriented discrete-time voltage controller design for grid-forming inverters”, IEEE Energy Conversion Congress and Exposition (ECCE), (2019)

[43] 美見勉・原辰次・近藤良：「基礎ディジタル制御」,コロナ社, (1988)

[44] Synopsis: https://www.synopsys.com/ja-jp/verification/virtual-prototyping/saber/saber-rd.html

Acknowledgements

I would like to express deep and sincere appreciation to Prof. Toshiji Kato and Prof. Kaoru Inoue of Doshisha University for their invaluable guidance, advice, and support regarding the research activities and others since I entered the Electric Circuit Laboratory in April 2016. They opened my eyes to control engineering and power electronics studies. It would not be possible without the support of them who believed in me and valued my work.

I also would like to thank every member of the Electric Circuit Laboratory for the 3 years we studied together. Special thanks go to my team, Shunya Sano, Akinobu Kaneko, Sota Yano, Daiki Yamashita, and Kosei Watanabe. We discussed and worked hard together and they supported me a lot to write this thesis.

Further, I appreciate that YANMAR HOLDINGS permitted my proceeding of doctoral course and supported me for the 3 years. Mr. Kengo Sasahara, Mr. Hitoshi Adachi, Mr. Takatomi Miyakubo, Mr. Kenji Ogata, and Mr. Yuya Kuroiwa should be specially thanked. I also would like to express gratitude to Dr. Akifumi Yamanaka, who has been sharing much time since we entered Doshisha University and we has encouraged each other to challenge the doctoral course.

Last but not least, I would like to express my deepest gratitude to my family, my parents and my wife Hitomi for their love, support, and understanding. They always encourage me to pursue my own dream.

Ko OUE